STAR-FORMING BLUE ETGS IN TWO NEWLY DISCOVERED GALAXY OVERDENSITIES IN THE HUDF AT $z = 1.84$ AND 1.9: UNVEILING THE PROGENITORS OF PASSIVE ETGS IN CLUSTER CORES

SIMONA MEI[1,2,3], CLAUDIA SCARLATA[4], LAURA PENTERICCI[5], JEFFREY A. NEWMAN[6], BENJAMIN J. WEINER[7],
MATTHEW L. N. ASHBY[7], MARCO CASTELLANO[5], CHISTOPHER J. CONSELICE[8], STEVEN L. FINKELSTEIN[10], AUDREY GALAMETZ[5,14],
NORMAN A. GROGIN[9], ANTON M. KOEKEMOER[9], MARC HUERTAS-COMPANY[1,2], CATERINA LANI[8,13], RAY A. LUCAS[9],
CASEY PAPOVICH[11], MARC RAFELSKI[3,12], AND HARRY I. TEPLITZ[3]

[1] GEPI, Observatoire de Paris, CNRS, University of Paris Diderot, Paris Sciences et Lettres (PSL), 61, Avenue de l'Observatoire F-75014, Paris, France
[2] University of Paris Denis Diderot, University of Paris Sorbonne Cité (PSC), F-75205 Paris Cedex 13, France
[3] Infrared Processing and Analysis Center, California Institute of Technology, Pasadena, CA 91125, USA
[4] Minnesota Institute for Astrophysics, School of Physics and Astronomy, University of Minnesota, Minneapolis, MN 55455, USA
[5] INAF, Osservatorio Astronomico di Roma, Via Frascati 33, I-00040 Monteporzio, Italy
[6] University of Pittsburgh, 3941 O'Hara St., Pittsburgh, PA 15260, USA
[7] Steward Observatory, University of Arizona, 933 N. Cherry St., Tucson, AZ 85721, USA
[8] School of Physics and Astronomy, University of Nottingham, Nottingham, NG7 2RD, UK
[9] Space Telescope Science Institute, Baltimore, MD, USA
[10] The University of Texas at Austin, 2515 Speedway, Stop C1400, Austin, TX 78712, USA
[11] George P. and Cynthia Woods Mitchell Institute for Fundamental Physics and Astronomy, Texas A&M University, 4242 TAMU, College Station, TX 78743, USA
[12] NASA Postdoctoral Program Fellow, Goddard Space Flight Center, Code 665, Greenbelt, MD 20771, USA
[13] School of Physics and Astronomy, Tel Aviv University, Tel Aviv 69978, Israel
[14] Max-Planck-Institut für Extraterrestrische Physik (MPE), Postfach 1312, D-85741 Garching, Germany

ABSTRACT

We present the discovery of two galaxy overdensities in the *Hubble Space Telescope* UDF: a proto-cluster, HUDFJ0332.4-2746.6 at $z = 1.84 \pm 0.01$, and a group, HUDFJ0332.5-2747.3 at $z = 1.90 \pm 0.01$. Assuming virialization, the velocity dispersion of HUDFJ0332.4-2746.6 implies a mass of $M_{200} = (2.2 \pm 1.8) \times 10^{14} M_\odot$, consistent with the lack of extended X-ray emission. Neither overdensity shows evidence of a red sequence. About 50% of their members show interactions and/or disturbed morphologies, which are signatures of merger remnants or disk instability. Most of their ETGs have blue colors and show recent star formation. These observations reveal for the first time large fractions of spectroscopically confirmed star-forming blue ETGs in proto-clusters at $z \approx 2$. These star-forming ETGs are most likely among the progenitors of the quiescent population in clusters at more recent epochs. Their mass–size relation is consistent with that of passive ETGs in clusters at $z \sim 0.7-1.5$. If these galaxies are the progenitors of cluster ETGs at these lower redshifts, their size would evolve according to a similar mass-size relation. It is noteworthy that quiescent ETGs in clusters at $z = 1.8-2$ also do not show any significant size evolution over this redshift range, contrary to field ETGs. The ETG fraction is $\lesssim 50\%$, compared to the typical quiescent ETG fraction of $\approx 80\%$ in cluster cores at $z < 1$. The fraction, masses, and colors of the newly discovered ETGs imply that other cluster ETGs will be formed/accreted at a later time.

Key words: galaxies: clusters: general – galaxies: evolution

1. INTRODUCTION

Galaxy clusters are the largest structures observed in the universe. Their distribution and (baryonic and dark) matter content constrain the cosmological model, and the study of their galaxy properties reveals the influence of dense environments on galaxy evolution.

Galaxies in clusters typically show a predominant early-type population and a red sequence (old stellar population) up to a redshift of z ≈1.5−2 (e.g., Kodama et al. 2007; Mei et al. 2009; Papovich et al. 2010; Andreon & Huertas-Company 2011; Snyder et al. 2012; Stanford et al. 2012; Zeimann et al. 2012; Gobat et al. 2013; Muzzin et al. 2013; Mantz et al. 2014). Most of the clusters observed in the local universe have assembled their current early-type galaxy population at those redshifts (e.g., Cohn & White 2005; Li et al. 2007; Chiang et al. 2013). The redshift range around $z \approx 1.5-2$, however, has remained largely unexplored until recently. The reason is that surveys based on cluster X-ray emission or the Sunyaev–Zel'dovich effect (SZ) lack depth and/or area to reach detections of typical clusters at these redshifts, and ground-based optical

spectroscopy would require excessive exposure times to confirm them spectroscopically when detected in the infrared/far-infrared bandpasses.

In the past five years, cluster samples at $z > 1.5$ have been significantly enlarged by the advent of deep and large enough surveys in the infrared and mid-infrared, such as GOODS-MUSIC (Castellano et al. 2007), the IRAC Distant Cluster Survey (IDCS; Eisenhardt et al. 2008; Stanford et al. 2012; Zeimann et al. 2012), the *Spitzer* Deep, Wide-field Survey (Ashby et al. 2009), the *Spitzer* SPT Deep Field (Ashby et al. 2013a), the *Spitzer* Adaptation of the Red-sequence Cluster Survey (SpARCS; Muzzin et al. 2013), *Spitzer* Wide-Area Infrared Extragalactic (Papovich et al. 2010), and the Clusters Around Radio-loud active galactic nucleus (AGN) program (Galametz et al. 2012; Wylezalek et al. 2013). Other cluster candidates have been identified around low-luminosity radio sources (Chiaberge et al. 2010). Spectroscopic capability to confirm redshifts has been enhanced by optical and infrared grism spectroscopy with the Wide Field Camera 3 (WFC3) on the *Hubble Space Telescope* (*HST*), and infrared ground-based multi-object spectroscopy with the Very Large Telescope

(VLT)/KMOS (Sharples et al. 2006), the Keck MOSFIRE (McLean et al. 2008, 2012), and the SUBARU MOIRCS (Ichikawa et al. 2006) instruments.

Until now, most clusters detected at $z > 1.5$ have been identified as overdensities of red galaxies (e.g., Gladders & Yee 2000), then confirmed by the spectroscopic follow-up of at least five members within 2 Mpc (e.g., Castellano et al. 2007, 2011; Kurk et al. 2009; Papovich et al. 2010; Tanaka et al. 2010; Stanford et al. 2012; Zeimann et al. 2012; Muzzin et al. 2013), and/or by their X-ray emission (Andreon et al. 2009; Gobat et al. 2011; Santos et al. 2011). Four clusters have been spectroscopically confirmed at $z \sim 1.8-2$: JKCS 041 (Andreon et al. 2009; Newman et al. 2014), IDCS J1426+3508 (Stanford et al. 2012), IDCS J1433.2+3306 (Zeimann et al. 2012), and CL J1449+085 (Gobat et al. 2011, 2013; Andreon & Huertas-Company 2011). For all of the clusters with $z > 1.8$, spectroscopic redshifts have been obtained with grism spectroscopy from *HST*/WFC3, after ground-based optical spectroscopy failed to obtain enough signal. These systems show large fractions ($\approx 50\%$) of star-forming galaxies, indicating that most of the quenching of star formation observed at lower redshift had not yet occurred (Tran et al. 2010; Fassbender et al. 2011; Hayashi et al. 2011; Tadaki et al. 2012; Zeimann et al. 2012; Brodwin et al. 2013). Recent observations at these redshifts also suggest that the specific star formation of galaxies in dense regions becomes higher than that in the field, although not all results are consistent with the supposed reversal of the star-formation density relation (Elbaz et al. 2007; Cooper et al. 2008; Grützbauch et al. 2011; Hatch et al. 2011; Popesso et al. 2012; Andreon et al. 2014; Gobat et al. 2013; Koyama et al. 2013; Strazzullo et al. 2013; Scoville et al. 2013; Tanaka et al. 2013; Ziparo et al. 2014; Santos et al. 2014).

Current X-ray and SZ observations probe cluster virialization through the detection of the hot gas in the gravitational potential well, down to cluster masses of $\approx 10^{14}\,M_\odot$ and up to a redshift of $z \approx 1$. At higher redshifts, only the extreme end of the cluster mass function can be detected by current instruments. A few objects at $1.5 < z < 2$ correspond to significant X-ray detections and were identified as already virialized (Andreon et al. 2009; Gobat et al. 2011; Santos et al. 2011; Stanford et al. 2012; Mantz et al. 2014). Two of them also show a significant SZ signal (Brodwin et al. 2012; Mantz et al. 2014). Their cluster masses cover the range of $M_{200} \approx (0.5-4) \times 10^{14}\,M_\odot$. The other detections (e.g., less massive objects) can only currently be identified as significant (passive or active) galaxy overdensities, without confirmation of virialization by the detection of hot gas. Depending on the presence, or not, of the red sequence and their richness, these objects have been identified as clusters or proto-clusters (e.g., Pentericci et al. 2000; Miley et al. 2004, 2006; Venemans 2007; Kuiper et al. 2010; Hatch et al. 2011). In this paper, we will use the term proto-cluster to mean a cluster in formation, in agreement with this literature. In our definition, a cluster in formation, or proto-cluster, is either (1) a cluster that has not yet formed a red sequence and, as a consequence, is detected as an overdensity of star-forming galaxies, or (2) a cluster that has not yet assembled and whose galaxies are distributed in groups that eventually will collapse to form a cluster (e.g., Chiang et al. 2013). Depending on the object richness/mass a galaxy overdensity is defined as group or cluster. Numerical simulations show that 90% of dark matter halos with masses of $M_{200} \geqslant 10^{14}\,M_\odot$ are a very regular virialized population up to a redshift of $z \sim 1.5$ (Evrard et al. 2008), and many works define galaxy overdensities that have at least this mass as clusters. However, some other works define groups up to $M \leqslant$ few $10^{14}\,M_\odot$ (e.g., Yang et al. 2007), and the definition of galaxy overdensities as a group or cluster varies in the literature. In this work, we will use the definition of clusters as overdensities with a mass of $M \geqslant 5 \times 10^{13}\,M_\odot$ because in previous studies of clusters at $z > 1.5$ objects in this mass range have been defined as clusters in formation, or proto-clusters (e.g., Papovich et al. 2010). In fact, halos of this mass range, at $z \sim 1.5$, will most probably be accreted in clusters with masses of $M > 10^{14}\,M_\odot$ at $z < 0.5$ (e.g., Chiang et al. 2013; Cautun et al. 2014).

Concerning the build-up of their early-type population, various studies have focused on the evolution of galaxies in clusters/dense environments from $z \approx 2$ to the present and compared it to the field (Rettura et al. 2010; Cooper et al. 2012; Mei et al. 2012; Papovich et al. 2012; Raichoor et al. 2012; Bassett et al. 2013; Huertas-Company et al. 2013a, 2013b; Lani et al. 2013; Newman et al. 2014; Poggianti et al. 2013; Shankar et al. 2013; Strazzullo et al. 2013; Vulcani et al. 2013; Delaye et al. 2014; Shankar et al. 2014). These results indicate that the median/average passive ETG sizes in clusters are larger (within $\sim 2\sigma$) and the analysis of the population with larger sizes suggests a different morphological type (E, S0) fractions and/or recently quenched faint galaxies.

In this paper, we present the discovery of two galaxy overdensities at redshifts of $z = 1.84$ and $z = 1.9$ in the *HST* Ultra-deep Field (HUDF; Beckwith et al. 2006) with observations from the Cosmic Assembly Near-infrared Deep Extragalactic Legacy Survey (CANDELS; PI: S. Faber, H. Ferguson; Grogin et al. 2011; Koekemoer et al. 2011) and the 3D *HST* survey (PI: P. van Dokkum; Brammer et al. 2012; van Dokkum et al. 2013). In Section 2, we present the observations. In Section 3, we describe our spectroscopic sample selection. In Section 4, we present the newly discovered overdensities and estimate one structure's mass. In Section 5, we study the stellar population and structural properties of their galaxies. In Section 6, we conclude and, in Section 7, we summarize our results.

We adopt a ΛCDM cosmology, with $\Omega_m = 0.3$, $\Omega_\Lambda = 0.7$, and $h = 0.72$. All magnitudes are given in the AB system (Oke & Gunn 1983; Sirianni et al. 2005). Stellar masses are estimated with a Chabrier initial mass function (Chabrier 2003).

2. OBSERVATIONS

The HUDF (Beckwith et al. 2006) is a $200'' \times 200''$ area with the deepest *HST* observations in multiple wavelengths. HUDF has been observed by several programs since the first *HST* Advanced Camera for Surveys (ACS) data release in 2004, including deep WFC3 images as part of the HUDF09 program (PI: G. Illingworth; Bouwens et al. 2011), CANDELS, 3D-*HST*, and HUDF12 (PI: R. Ellis; Ellis et al. 2013; Koekemoer et al. 2013). CANDELS is a 902-orbit Multi-cycle Treasury survey with the *HST*, completed in Cycle 20. The main instrument used by the survey is WFC3, with three, four, and six orbit exposures in imaging with the WFC3/F105W (Y_{105}), F125W (J_{125}), and F160W (H_{160}) filter, respectively, and grism spectroscopy in the infrared (WFC3/IR) channel. Parallel observations were undertaken with the ACS. A combination of all the HUDF observations with ACS and WFC3 has been

recently released by the eXtreme Deep Field (XDF) program (Illingworth et al. 2013). We will use the combined XDF images for the galaxy structural properties analysis, in particular, imaging with ACS/WFC F775W, F814W, and F850LP (i_{775}, I_{814}, and z_{850}, respectively), for a total exposure time of 377.8 ks, 50.8 ks, and 421.6 ks, respectively, and WFC3/IR J_{125} and H_{160} for a total exposure time of 112.5 ks and 236.1 ks, respectively. The ACS WFC resolution (pixel size) is $0\!\!''05$/pixel, and its field of view (FOV) is $202''$ x $202''$. WFC3/IR has a $136''$ x $123''$ FOV, with a spatial resolution of $0\!\!''13$/pixel. The images have been drizzled and registered to obtain ACS and WFC3 mosaic images with the same resolution of $0\!\!''06$. The image reduction is described in detail in Illingworth et al. (2013). We have verified that our results do not change when using the HUDF12 release (Koekemoer et al. 2013).

For the spectroscopy, the HUDF has been observed by two *HST* Treasury programs with spectroscopic observations: the CANDELS and the 3D-*HST* program. The 3D-*HST* program, completed in Cycle 19, obtained deep spectroscopy of the HUDF with the WFC3/IR G141 grism. The grism spectroscopy from these two programs was recently released as combined reduced spectra that include 8 orbits of 3D-*HST* and 9 orbits of CANDELS supernova follow-up observations, for a total of 17 orbits of observations (Brammer et al. 2012). The WFC3/IR G141 grism has an efficiency larger than 30% in the wavelength range $1.1 < \lambda < 1.65\,\mu m$, a spatial resolution of $0\!\!''13$/pixel and a dispersion of 46.5 Å pixel^{-1}. Typical uncertainties are 5Å for the zero point and 0.04Å for the dispersion (Kuntschner et al. 2010). The spectra were extracted by independent software developed by the 3D-*HST* collaboration, as described in Brammer et al. (2012), and redshifts have been estimated using both grism spectroscopy and broadband photometry for a combined spectro-photometric estimate. For the entire spectroscopic catalog, spectral features used to estimate redshifts include rest-frame Hα, [O II]$\lambda3727$, [O III]$\lambda5007$ emission lines, and the Balmer 4000Å break. The 3D-*HST* spectroscopy covers an area of $\sim140'' \times 140''$ in the HUDF.

Near ultra-violet images (NUV) of the HUDF were obtained in a Hubble Space Telescope treasury program (hereafter UVUDF; Teplitz et al. 2013) using the WFC3/UVIS detector. This project obtained deep images of the HUDF in the F225W, F275W, and F336W filters. Data were obtained in two observing modes (as described in Teplitz et al. 2013), with ~15 orbits of integration per filter in each mode. For the current analysis, we use the half of the data that were obtained with the post-flash (the UVIS capability to add internal background light), to mitigate the effects of degradation of the charge transfer efficiency of the detectors (MacKenty & Smith 2012). The data were reduced using a combination of standard and custom calibration scripts (see M. Rafelski et al. 2014, in preparation), including the use of newly released software to correct for charge transfer inefficiency. The individual reduced exposures were then registered and combined following the methods developed for CANDELS (Koekemoer et al. 2011). The 5σ rms sensitivities in an aperture with $0\!\!''2$ radius are 27.9, 27.9, and 28.3 mag in $F225W$, $F275W$, and $F336W$, respectively. Photometry in the UV was measured in isophotal areas determined from the B-band detection image obtained with SExtractor in dual image mode (Bertin & Arnouts 1996).

3. SPECTROSCOPIC SAMPLE SELECTION

Using the CANDELS and 3D-*HST* spectroscopic redshifts, we identified an initial galaxy overdensity in the HUDF at redshift $z \approx 1.85$. We explain below how we identified and quantified this detection.

To assess the quality of the spectra, we used both visual inspection, the published spectro-photometric analysis from the 3D-*HST* collaboration (Brammer et al. 2012), and the CANDELS Guo et al. (2013) photometric redshift catalog. For 3D-*HST* spectroscopy, we applied the shift $z_{\rm spec} = 0.005 \times (1 + z_{\rm 3DHST})$, as suggested in the documentation of the 3D-*HST* data release (van Dokkum et al. 2013, 3D-*HST* data release documentation). The accuracy of the Guo photometric redshifts is estimated to be $\delta_{z_{pz}} = 0.030 \times (1 + z)$ for $H_{160} < 24$ mag and $\delta_{z_{pz}} = 0.039 \times (1 + z)$ for $H_{160} > 24$ mag, with a global outlier fraction of $\approx4\%$. This gives typical photometric redshift errors of $\sigma_{pz} = 0.09-0.1$ at $z = 1.8-1.9$ up to $H_{160} \approx 26$ mag. The Guo et al. (2013) catalog covers the HUDF area (~4.6 arcmin^2), and extends to the CANDELS/GOODS-S field, in the deep (~55 arcmin^2) and wide (~30 arcmin^2) CANDELS surveys. The Guo et al. photometric catalog has a 5σ magnitude depth of 27.4, 28.2, and 29.7 AB, for an aperture of $0\!\!''17$, in the CANDELS wide, deep, and HUDF fields, respectively.

We (BW first and then SM verified and agreed) flagged each spectrum as (1) certain, (2) good independently of photometric redshift estimates, (3) good using photometric redshift estimates, (4) probable, and (5) not usable. For this work, we only use certain and good spectroscopic grism redshifts (flags 1–3). We have been particularly attentive to the possible contamination from misidentification of Hα emission as O III, from the foreground cluster at $z = 1.096$ (Salimbeni et al. 2009), e.g., we have not considered two galaxies because they show a single line emission and their photometric redshifts would indicate a most probable redshift at $z \sim 1$. The lines detected with significant signal-to-noise ratios (S/Ns) are specified in Table 1, and are mainly [O III]$\lambda5007$ or the O III doublet, and [Hβ]$\lambda4861$.

We found 24 galaxies, which all lie within a radius of $R = 2'$ (that corresponds to a comoving radius of 1 Mpc at $z \approx 1.8-1.9$) of the main overdensity center (see below), and have good quality spectra from which we measure redshifts in the range $1.8 < z < 1.95$. In this range, the grism redshift median statistical uncertainty is ≈0.001 (Brammer et al. 2012; Colbert et al. 2013). To the statistical uncertainty, we add a systematic of $0.003 \times (1 + z_{\rm spec})$. We estimate the systematics from the median scatter when comparing spectroscopic redshifts measured by the CANDELS collaboration (BW) with spectro-photometric redshifts published by the 3D-*HST* collaboration (Brammer et al. 2012), in the redshift range $z = 0.5-2.5$. This systematic is larger than, but consistent with, the uncertainties obtained from the simulations by Colbert et al. (2013) and exactly the same as found by Gobat et al. (2013).

We searched the entire GOODS CDF-S master catalog[15] for spectroscopy from ground-based follow-up of the area. When grism redshifts are probable or not usable, and ground-based multiple line redshift measurements are available with an average S/N per pixel >3 (Kurk et al. 2013), we use VLT/

---

[15] http://www.eso.org/sci/activities/garching/projects/goods/MasterSpectroscopy.html

Table 1
Photometric Redshift Overdensities

Name	R.A. (deg.)	Decl. (deg.)	$H_{160}^{\lim}$	$N_{\rm gal}$	$N_{\rm spec}, \bar{z}_{\rm spec}$	S/N	R(arcmin.)
HUDFJ0332.4-2746.6	53.15565	−27.77930	24.5	8	7	⋯	
Group 1	53.11842	−27.78338	24.5	6	5,1.89 ± 0.01	5	1.9
Group 2	53.11615	−27.87192	24.5	6	⋯	5	5.9
Group 3	53.19252	−27.82862	24.5	5	3,1.88 ± 0.03	4	3.5
HUDFJ0332.4-2746.6	53.15565	−27.77930	26	13	2	⋯	
Group 1	53.11842	−27.78338	26	13	5,1.89 ± 0.01	2	1.9
Group 2	53.11615	−27.87192	26	14	⋯	2	5.9
Group 4	53.09392	−27.76772	26	18	6,1.88 ± 0.02	3	3.3
Group 5	53.18884	−27.72558	26	15	4,1.95 ± 0.01	2	3.7
Group 6	53.14208	−27.81992	26	14	8,1.87 ± 0.02	2	2.5

Note. This Table shows properties of the photometric redshift overdensity in the GOODS-S field, with photometric redshifts consistent with the HUDFJ0332.4-2746.6 and HUDFJ0332.5-2747.3 spectroscopic redshifts. $H_{160}^{\lim}$ is the magnitude limit we have used in our overdensity search, R.A. and decl. are the position of the ovserdensity center, $N_{\rm gal}$ the number of galaxies selected within 1′ for each overdensity, $N_{\rm spec}$ the number of galaxies with good quality spectroscopic redshifts in the range of $1.8 < z_{\rm spec} < 2$, and their average value, S/N is the overdensity significance, as defined in the text, and R is the distance from the HUDFJ0332.4-2746.6 center. Group 1 and Group 4, and Group 1 and Group 6 have one galaxy in common, respectively.

FORS2 redshift measurements instead of the grism spectroscopy. Eight galaxies with redshifts in the range of $1.8 < z < 1.95$ have good quality GMASS VLT/FORS2 spectroscopy and respect our S/N criteria, and four have better quality than the grism spectra. We added the missing 4 to the 24 galaxies above, to obtain 28 galaxies with good quality spectra in the range of $1.8 < z < 1.95$. The 3D-*HST* spectra of the cluster members were published by the 3D-*HST* collaboration (Brammer et al. 2012). The GMASS spectra were published in Kurk et al. (2013).

The selected spectroscopic members extend to magnitudes as faint as $H_{160} \approx 25.7$ mag; however, the grism spectroscopy sample shows a marked decrease in number at magnitudes fainter than $H_{160} \approx 24.5$ mag. At this magnitude, ≈95% of the CANDELS galaxies in the HUDF area (Guo et al. 2013) have a grism redshift estimation, and ≈50% have good quality flags from our classification above.

The UVUDF NUV images permitted us to confirm that the selected galaxies are at $z \sim 1.8$–1.9, since we expect them to be UVIS/*F*225*W* dropouts (see Teplitz et al. 2013) and to be detected in the *F*336*W* filter. Each candidate has been inspected visually and independently by two of us (CS and SM). Two of the candidates, UDF-1898 and UDF-1909 are *F*336*W* dropouts, and could either be galaxies at higher redshift or too faint to be detected. We will not consider these two objects in the rest of our analysis, leaving 26 selected galaxies with redshifts of $1.8 < z_{\rm spec} < 1.95$. In the Appendix, we show the WFC3 *F*225*W*, *F*275*W*, *F*336*W*, and ACS *F*435*W*, I_{814} and WFC3 J_{125} images for each candidate.

We describe in Table 1 all of the selected galaxies, and identify them by their 3D-*HST* UDF ID (Brammer et al. 2012) or GMASS ID (Kurk et al. 2013).

4. NEWLY DISCOVERED OVERDENSITIES IN THE UDF

### 4.1. Structure Definition Using Spectroscopy

As shown in Figure 1, the redshifts of the 26 selected galaxies appear to follow a double Gaussian distribution. This is confirmed by a classical Kolmogorov–Smirnov test, skewness and kurtosis test and the two more robust asymmetry index (A.I.) and tail index (T.I.) described in Bird & Beers

(1993; as in, e.g., Castellano et al. 2011). The tests were applied on each Gaussian separately (e.g., we only considered redshifts within 3σ from each mean for each test). For the structure at $z = 1.84$, we obtained a skewness of 0.05 ± 0.10, a kurtosis of -0.49 ± 0.17, a T.I. of 1.4 ± 0.1, and an A.I. of $-0.2 + / -0.5$. For the structure at $z = 1.9$, we obtained a skewness of -0.9 ± 0.4, a kurtosis of -0.5 ± 0.9, an A.I. of -0.4 ± 0.5, and the T.I. could not be calculated with so few points. We estimated uncertainties with a Monte Carlo simulation. All parameters are consistent with a random population extracted from a Gaussian distribution (Bird & Beers 1993).

To select the structure members, given the small number of galaxies, we fit a double Gaussian plus a background to the observed distributions. We took into account Poissonian uncertainties in the histogram and adopted a redshift bin of 0.01. The Gaussian fits give $\bar{z} = 1.84 \pm 0.01$ and $\bar{z} = 1.905 \pm 0.005$, for the first and second structure, respectively. We obtain $\bar{z} = 1.84 \pm 0.01$ and $\bar{z} = 1.90 \pm 0.01$, respectively, from a biweight mean redshift and standard deviation.

Selecting galaxies within $3 \times \sigma_{\bar{z}}$ of the two means, we obtained 18 spectroscopic members for the first Gaussian and 7 spectroscopic members for the second. One galaxy is not selected as part of the structures because its redshift is too low.

To better estimate the significance of the two redshift overdensities, since we do not have a large area, we will measure statistics in redshift bins in the HUDF area covered by the grism spectroscopy, that corresponds to a co-moving size of ∼1 Mpc. We used the complete sample of certain and good (as defined above) spectroscopic grism redshifts from CANDELS and 3D-*HST* in the range $1.2 < z < 2$, and calculated both projected densities using Nth-nearest neighbor distances and galaxy overdensities, following Papovich et al. (2010; see also Gobat et al. 2013). In this redshift range, WFC3 redshifts are mainly obtained from Hα and O III emission lines combined with photometric redshifts as explained above. While it is true that to have a precise estimate of the overdensities, we would need to use spectroscopic samples at the same redshift over a large area, such a sample is currently not available. However, even if galaxies at different redshifts have redshift estimates
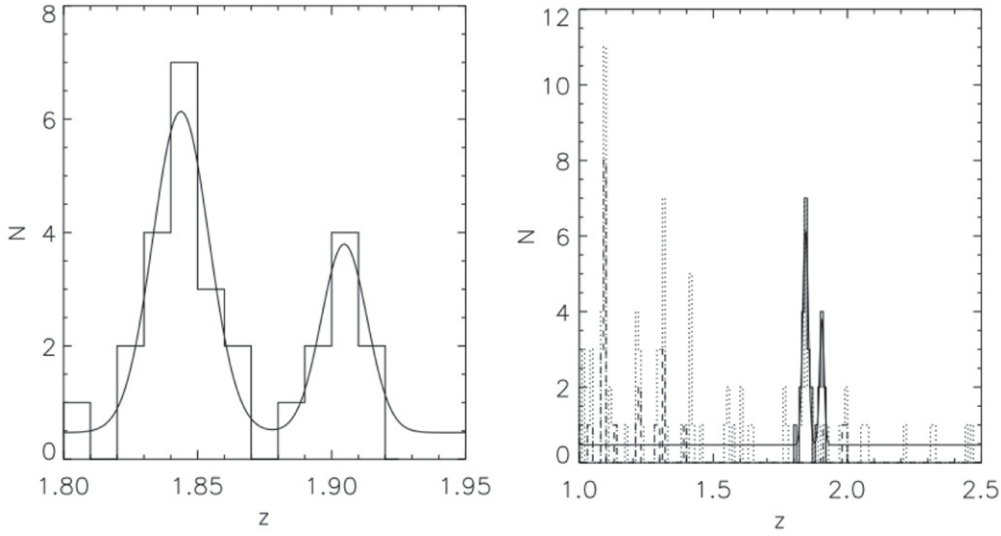
Figure 1. On the left, the redshift distribution of HUDFJ0332.4-2746.6 and HUDFJ0332.5-2747.3 spectroscopic members. The continuous line is the double Gaussian fit described in the text. On the right, we also show the spectroscopic redshift distribution in the HUDF from the 3D-*HST* (dashed line) and the GOODS and GMASS catalogs (dotted line).

based on different emission lines, e.g., Hα and O III, and the flux limit increases with redshift, these two effects would point to a lower limit for our O III emission line overdensities, since (1) they would be at the higher redshift end of the range in redshift that we considered and (2) they are defined by their O III emission and the O III emission has similar or lower strength than Hα (e.g., Colbert et al. 2013). We did not consider GMASS redshift measurements in this estimation, because our sample is dominated by emission line galaxies. In both calculations, we have considered all galaxies brighter than $H_{160} = 27$ mag.

For the first overdensity estimate, we measure projected densities using Nth-nearest neighbor distances defined as $\Sigma_N = \frac{N}{\pi D_N^2}$ (e.g., Dressler 1980). N is the number of neighbors, D_n is defined as the distance in Mpc to the Nth nearest neighbor. We have calculated Σ_N within redshift bins of amplitude 0.06 (e.g., within a distance in redshift space $3 \times \sigma_{\bar{z}}$ from the biweight analysis) from $z = 1.2$ to $z = 2$. The significance of our detections is estimated by taking the ratio: S/N $= \frac{\Sigma_N - \Sigma_N^{bck}}{\sigma_{\Sigma_N^{bck}}}$. Our background density estimates were stable in the range $N = 3$–7, with $\Sigma_N^{bck} = 0.5 \pm 1$. The structure at $z = 1.84$ is an overdensity at $\approx 20\sigma$ above the background density (stable for $N = 4$–7, it is $\approx 14\sigma$ at $N = 3$). The structure at $z = 1.9$ has a density at 6–8σ above the background density for $N = 3$ and 4, respectively. Given the smaller number of galaxies, this measurement is less stable at different N. Our results do not change if we enlarge the redshift range, and do not consider in the analysis the known cluster at $z = 1.096$ (see above).

For the second overdensity estimate, we use the definition of galaxy contrast $\delta_c = \frac{N_{gal} - N_{bkg}}{N_{bkg}}$. N_{gal} is the number of galaxies in a given redshift bin, and N_{bkg} is the average number of background galaxies in the entire redshift range of $1.3 < z < 2$. The significance of our detections is estimated by taking the ratio S/N $= \frac{N_{gal} - N_{bkg}}{\sigma_{bkg}}$. We obtain $N_{bkg} = 0.6 \pm 0.9$ galaxies per redshift bin of 0.06. Even if we do not count $>3\sigma$ peaks in the redshift distribution, this might be an upper limit to the average background, since we already know that there are significant

overdensities in this field (Salimbeni et al. 2009). For the first and second structure, we obtain a $\sim 18\sigma$ and a $\sim 6\sigma$ galaxy overdensity, respectively. These results are consistent with those from projected densities using Nth-nearest neighbor distances.

This analysis confirms the detection of the structure at $z = 1.84$ as a significant galaxy overdensity. We call this structure HUDFJ0332.4-2746.6, and adopt as the center the position of its brightest galaxy (UDF 2095, with $H_{160} = 22.008 \pm 0.002$ mag) in its spatially denser region of comoving size $R = 500$ kpc ($1'$ at this redshift), at [R.A., decl.] = [53.155647, −27.779298]. Only one member (GMASS 220) is farther than $R = 1'$ from this center. The measured overdensity is similar to that measured for red galaxy overdensities that were confirmed as galaxy clusters by their X-ray emission (Papovich et al. 2010; Gobat et al. 2011). Also, numerical simulations of our standard cosmological model (Hahn et al. 2007a, 2007b; Cautun et al. 2014) predict that galaxy overdensities of ~ 30 at $z \sim 2$ have a probability of $\sim 40\%$ of being a node of the cosmic web (e.g., a cluster or proto-cluster) and a probability of $\sim 10\%$ of being a filament. While predictions from Cautun et al. (2014) and Hahn et al. (2007a, 2007b) do not take into account projection effects, long filaments (we would need a filament with a comoving lenght of 50 Mpc seen in projection in the area of HUDFJ0332.4-2746.6 to reproduce our measured overdensity) at $z \sim 2$ account for only a very small percentage ($<10\%$ from Cautun et al. 2014) of the total finalement length distribution. The number of filaments decreases with the filament length, and dense and long filaments are also rare with a probability of $\sim 2 \times 10^{-4}$ of being found in the HUDF area (Figure 53 from Cautun et al. 2014). Therefore, HUDFJ0332.4-2746.6 has a higher probability of being a cluster of galaxies than a filament.

The second overdensity is detected at 4−7σ, and we will call it HUDFJ0332.5-2747.3. We adopt as the center the position of the brightest galaxy ($H_{160} = 22.463 \pm 0.002$ mag) in its spatially denser region, at [R.A., decl.] = [53.149298, −27.788534]. Numerical simulations of our standard cosmological model (Hahn et al. 2007a, 2007b; Cautun et al. 2014) predict that galaxy overdensities of ~ 10 at $z \sim 2$ have a
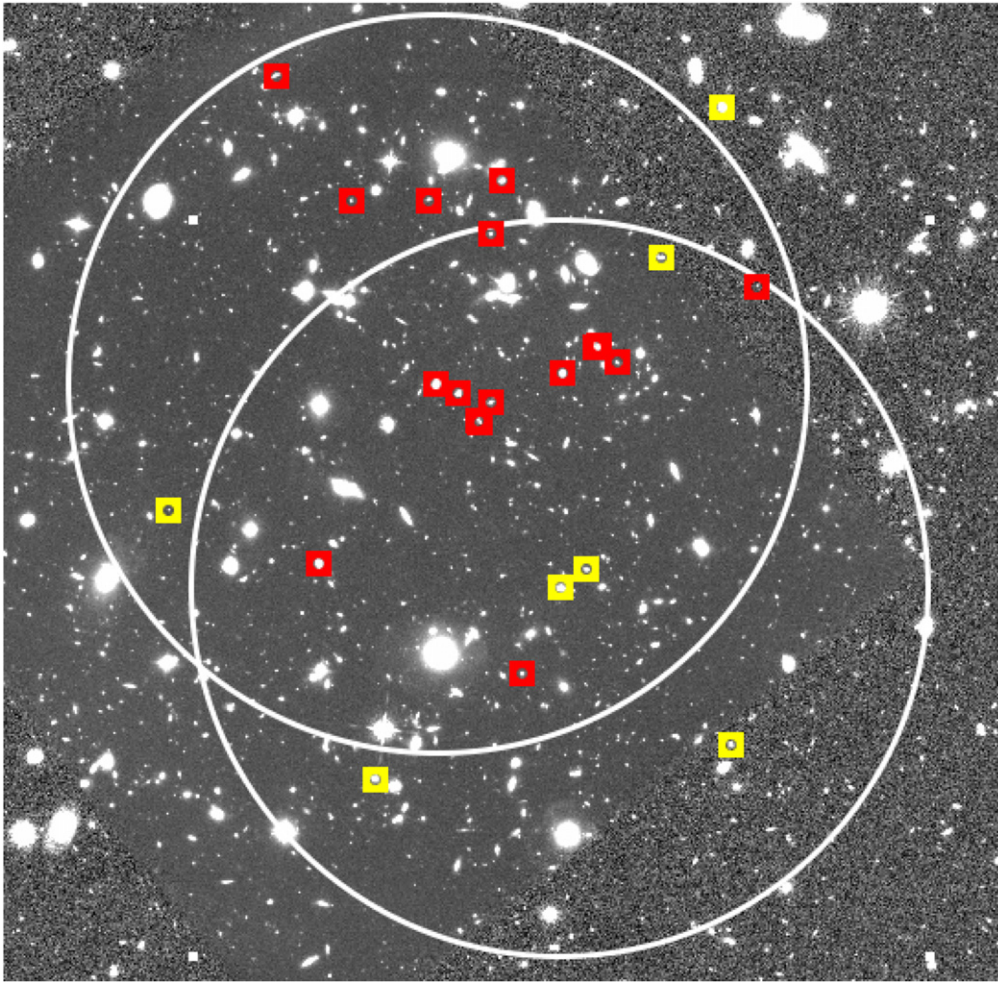
Figure 2. Our structures' galaxies. Over the H_{160} image of the HUDF, the red and yellow boxes show spectroscopic members for HUDFJ0332.4-2746.6 and HUDFJ0332.5-2747.3, respectively. Both UDF-2090 and UDF-2103, and UDF-2433 and UDF-2491, are pairs and cannot be distinguished in the figure. The large white circles, centered on each structure, have a radius of $R = 1'$, that corresponds to a comoving radius of ≈ 0.5 Mpc. Most of HUDFJ0332.4-2746.6 are within $1'$ from the structure center, the only exception is GMASS220. HUDFJ0332.5-2747.3 is more sparse. North is on the top, east is on the left.

probability of $<10\%$ of being a node of the cosmic web (e.g., a cluster or proto-cluster) and a probability of $\sim 50\%$ of being a filament. We identify this structure as a galaxy group because it is less populated and less compact and its detection threshold is closer to that of a galaxy group (e.g., Tanaka et al. 2013), but it also has a high probability of being a filament according to numerical simulations.

The positions of the structures' members are shown in Figure 2. The comoving distance between the two structures is ~ 100 Mpc. At $z \sim 2$, the standard cosmological model predicts that the comoving volume of progenitors of clusters with present masses $M > 10^{14} M_\odot$ can reach ~ 25 Mpc^3 for the most massive clusters (Chiang et al. 2013; Shattow et al. 2013), thus the two structures are not predicted to necessarily merge to form a present-day cluster.
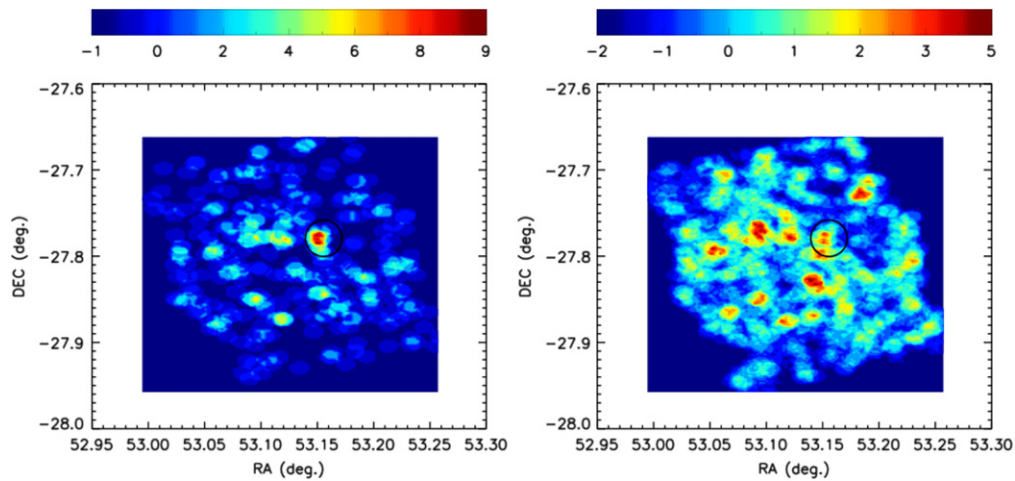
4.2. Photometric Redshift Overdensities

While the CANDELS and 3D-*HST* spectroscopic covers only the HUDF area, the Guo et al. (2013) photometric redshift catalog covers the entire GOODS-S field for a total area of ~ 170 arcmin^2. This means that when using photometric redshifts, we can extend our overdensity search over a comoving projected area of ~ 80 Mpc^2 at $z = 1.8-19$. We will

use these measurements to investigate if our overdensities are isolated or are part of a larger-scale overdensity distribution at the same redshift.

We have selected all galaxies with magnitudes brighter than $H_{160} = 24.5$, and 26 mag, which correspond to median uncertainties on the single photometric redshifts of $\lesssim 0.1$ and 0.15, respectively. Given the larger uncertainties associated with photometric redshifts, we measured overdensities in photometric redshift ranges at $\pm 1\sigma$ from the center of our larger overdensity, HUDFJ0332.4-2746.6. Given the uncertainties on photometric redshift we cannot separate HUDFJ0332.4-2746.6 from HUDFJ0332.5-2747.3 in this analysis. The redshift ranges that we considered for sample depths of $H_{160} = 24.5$ and 26 mag, are of $1.74 < z_{phot} < 1.94$ mag and $1.69 < z_{phot} < 1.99$ mag, respectively. In this last photometric redshift range, we estimated the purity and completeness of our photometric redshift catalog using the spectroscopic sample. We find it to be $\sim 70\%$ complete and $\sim 60\%$ pure.

We identified overdensities in regions of a projected comoving radius of 0.5 Mpc, as $\delta_c = \frac{N_{gal} - N_{bkg}}{N_{bkg}}$, and define S/N $= \frac{N_{gal} - N_{bkg}}{\sigma_{bkg}}$. Figure 3 shows the S/N of the overdensities

Figure 3. Photometric redshift overdensities at the same redshift as our spectroscopically detected overdensities (see the text for the exact photometric redshift range). On the left and the right, we show overdensities obtained at a depth of $H_{160} = 24.5$ mag and $H_{160} = 26$ mag, respectively. The black circles are centered on the HUDFJ0332.4-2746.6 center, and have a comoving radius of ~0.5 Mpc. In both cases, our structures are found as one single overdensity, and are part of a larger overdense structure that extends over a region of ~12 arcmin^2 (~6 Mpc^2, in comoving distance).

that we detected, and we list the most significant overdensities in Table 1, selecting all overdensities with the three highest S/Ns in each of two cases, and to always include HUDFJ0332.4-2746.6. At both depths, HUDFJ0332.4-2746.6 and two overdensities, that we called Group 1 and Group 2 are detected within the three highest S/Ns. As we expect from the median photometric redshift uncertainties, when we increase the depth in magnitude we also increase the background and the background noise, and our detections are less significant. We considered as a single detection all overdensities closer than a comoving distance of 0.5 Mpc. Group 1 is at a comoving distance of ~1 Mpc from HUDFJ0332.4-2746.6, and Group 4. UDFJ0332.4-2746.6 and HUDFJ0332.5-2747.3, with Group 1, Group 4, and Group 6 form a structure that extends to ~10′ ×10′ (~5 × 5 comoving Mpc). All Groups together cover a region of ~12′ ×12′ (~6 × 6 comoving Mpc).

In Figure 3, we show the overdensities. In Figures 4 and 5, we show the photometric and spectroscopic redshift histograms for each overdensity. In Table 1, we give the number of galaxies with $1.8 < z_{spec} < 2$ within 1.5′ from each overdensity center, and their average spectroscopic redshift. From the available spectroscopy, Group 1, Group 3, Group 4, and Group 6 have three to eight galaxies that show an average spectroscopic redshift for each structure close to HUDFJ0332.4-2746.6 and HUDFJ0332.5-2747.3 (see Table 1). All of these structures together show 19 galaxies within 3σ (observational scatter) from the red sequence measured in Mei et al. (2009) at $z \sim 1$, when it is passively evolved at $z = 1.84$. Group 5 has a higher average spectroscopic redshift from four galaxies, at $\bar{z}_{spec} = 1.95 \pm 0.01$. Given the few galaxies that are spectroscopically confirmed, we cannot analyze the groups in detail.

If confirmed as significant spectroscopic overdensities, some of the galaxies in these groups might be part of the same large-scale structure as HUDFJ0332.4-2746.6 or HUDFJ0332.5-2747.3, but without extensive spectroscopic follow-up, we cannot draw a firm conclusion. As thoroughly discussed in the literature (e.g., Shattow et al. 2013 and references therein), projection effects can strongly affect fixed aperture measurements of overdensities, especially when using high uncertainties in photometric redshifts. Our detections have to be

confirmed by spectroscopic follow-up for a better quantification of their significance.

4.3. HUDFJ0332.4-2746.6 Mass Estimate

4.3.1. X-Ray Observations

We checked the 3 Msec *XMM* and 4 Msec *Chandra* X-ray observations for both point sources associated with the galaxies in the two overdensities and for possible extended emission from the ICM.

The HUDFJ0332.4-2746.6 member UDF-2095 coincides with source #512 in the 4 Msec catalog (Xue et al. 2011). It has a soft band flux of 1.8×10^{-17} erg/sec/cm^2 and a hardness ratio of 0.27. The catalog classifies the emission as a *galaxy* so it is most probably associated with star formation rather than with AGN activity. There are other X-ray sources within the cluster region, of which one (#505 from Xue et al. 2011) is extended but associated with a lower redshift galaxy ($z = 0.99$). There is no indication of diffuse extended emission coinciding with either overdensity position.

From the lack of extended X-ray emission, we can place an upper limit on the X-ray luminosity of $1\text{-}6 \times 10^{43}$ erg s^{-1}, depending on the temperature assumed (in the range $T = 1\text{--}3$ KeV, respectively). If we use the cluster mass–luminosity derived by Rykoff et al. (2008), this corresponds to an upper limit in total mass of $M_{200} < 1 \times 10^{14} M_\odot$, and $M_{200} < 3 \times 10^{14} M_\odot$, for an upper limit in the X-ray luminosity of 1 and 6×10^{43} erg s^{-1}, respectively. This means that we cannot exclude that the most massive structure is a cluster with mass $M_{200} \sim 10^{14} M_\odot$.

4.3.2. Mass Estimates

From numerical simulations, we know that 90 % of the halos with masses of $M_{200} \geqslant 10^{14} M_\odot$ up to $z \sim 1.5$ have virialized (Evrard et al. 2008). Since we cannot exclude this hypothesis from our X-ray measurements (see the previous section), and an overdensity of galaxies at ~20σ can correspond to a halo of mass $M_{200} \sim 10^{14} M_\odot$ (e.g., Gobat et al. 2013), we decide to make this assumption. This is also supported by the fact that
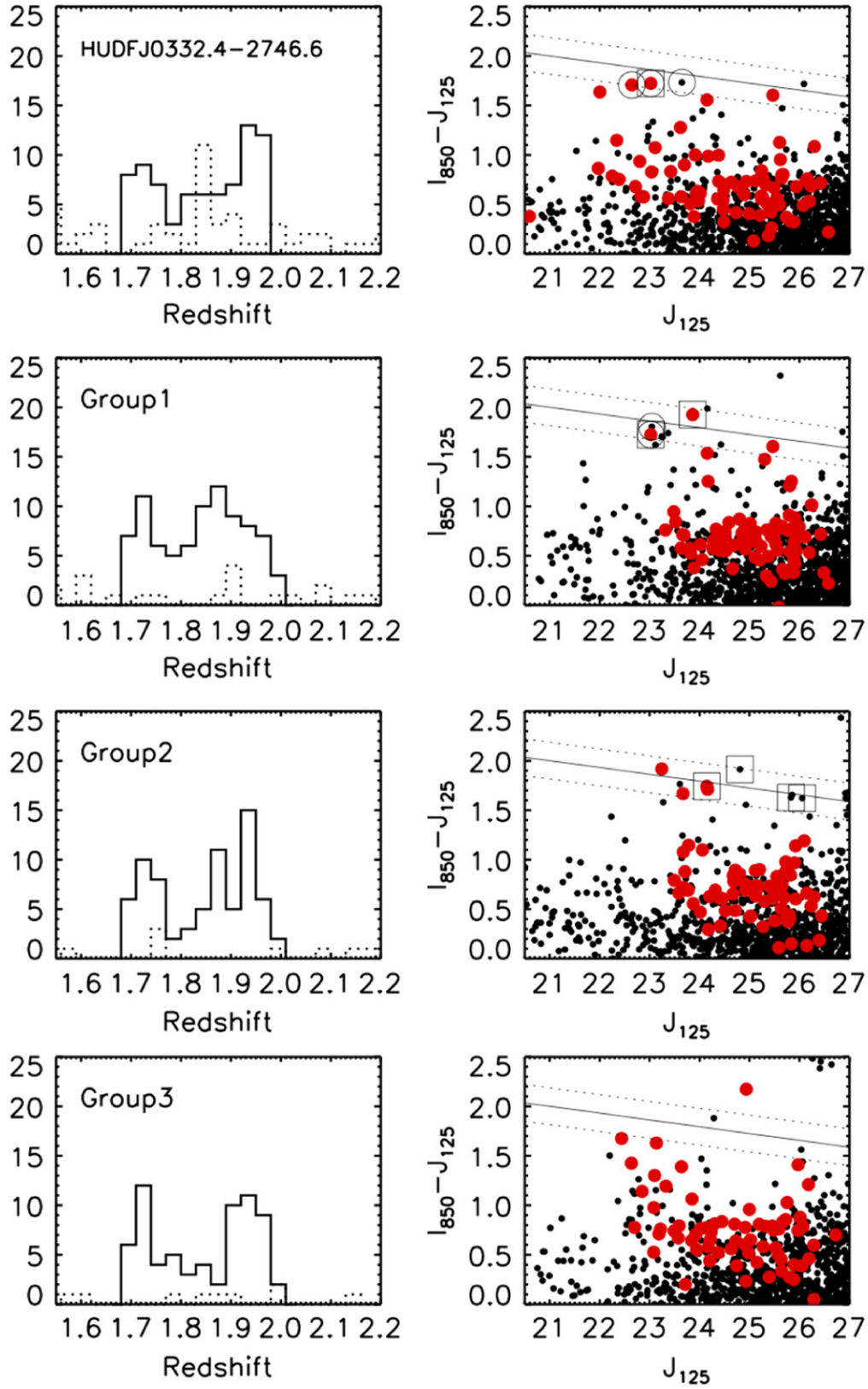
Figure 4. On the right, we show the histogram of the photometric redshift members (continuous line, $1.69 < z_{phot} < 1.99$) within $1\overset{.}{5}$ from the center of each photometric redshift overdensity in Table 1. The dotted histogram shows the distribution of galaxies with known spectroscopic redshifts. On the left, we show the color–magnitude relation for each overdensity. The $(I_{850} − J_{125})$ color is close to the $(U − B)$ rest-frame, and J_{125} to the B-band rest-frame at $z \sim 1.84$. The black points are all galaxies within $1\overset{.}{5}$ from the overdensity center. The larger red points are the galaxies with $1.69 < z_{phot} < 1.99$. The squares and circles around symbols indicate an AGN detection and a known spectroscopic redshift, respectively. The continous line shows the color–magnitude relation at $z \sim 1$ from Mei et al. (2009) passively evolved at $z = 1.84$, and the dashed lines show a region within three times the observed scatter. Some of the overdensities show a red sequence, even if none of the red sequence galaxies with known spectroscopic redshifts has spectroscopic redshifts within 3σ of HUDFJ0332.4-2746.6 and HUDFJ0332.5-2747.3 spectroscopic redshift.
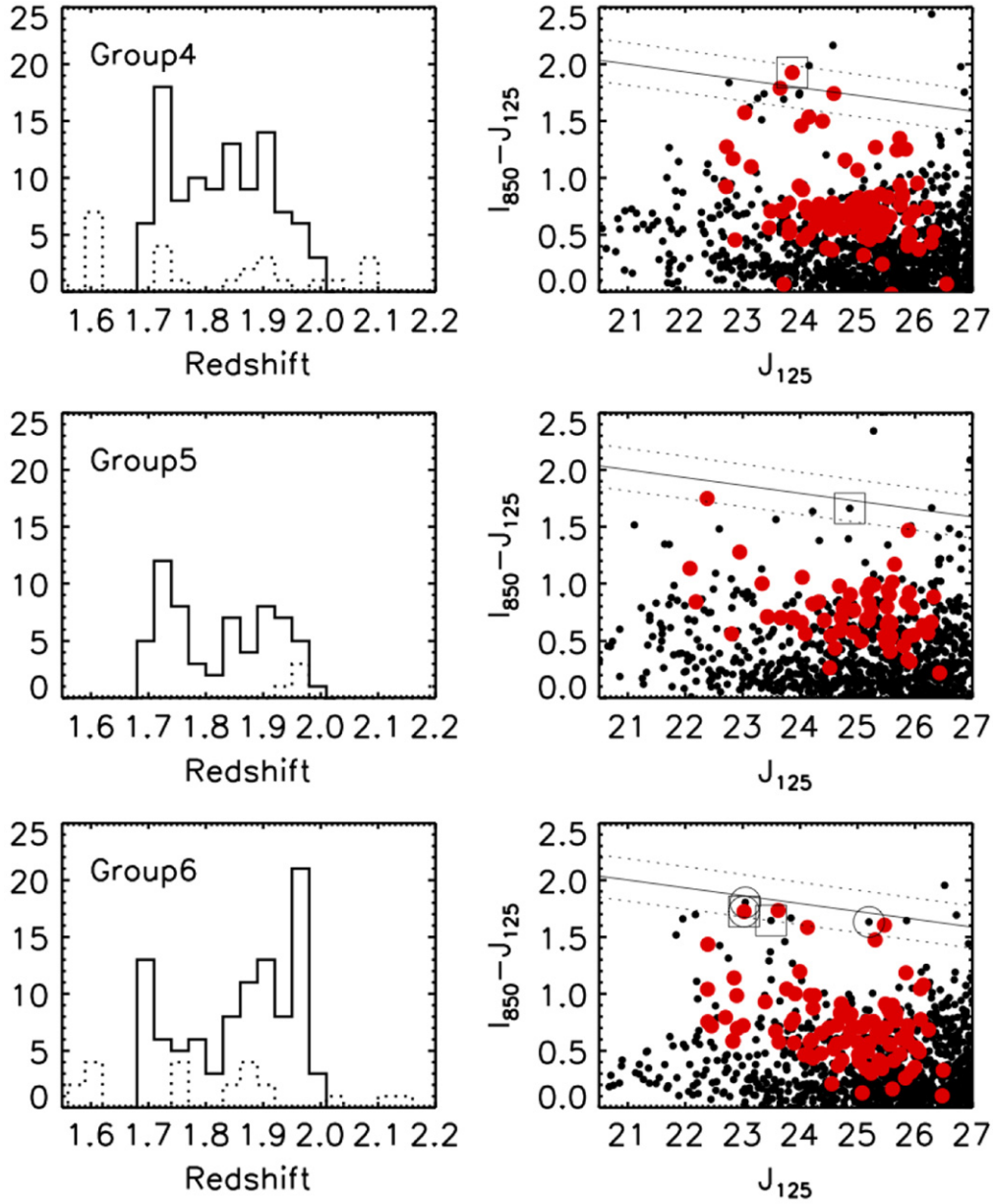
Figure 5. Same as Figure 4, but for the remaining groups from Table 1.

the velocity distribution of HUDFJ0332.4-2746.6 is consistent with a Gaussian, e.g., it has already separated from the Hubble flow (e.g. Nakamura 2000; Merrall & Henriksen 2003).

With this assumption, HUDFJ0332.4-2746.6 mass can be estimated from its velocity dispersion. The line-of-sight (LOS) cluster velocity dispersion can be highly anisotropic, and small samples lead to large systematic uncertainties (White et al. 2010). For HUDFJ0332.4-2746.6, we expect uncertainties in the velocity dispersion from anisotropies of ≈10%. We do not attempt to do the same for HUDFJ0332.5-2747.3, in fact, the uncertainty on the mass estimate for HUDFJ0332.5-2747.3 is too large because of the smaller number of galaxies, and we do not attempt to measure it.

We measure the HUDFJ0332.4-2746.6 intrinsic velocity dispersion from its 18 members, following Danese et al. (1980). We add in quadrature the statistical and systematic uncertainties in redshift. From the overdensity intrinsic velocity dispersion, we obtain an estimate of the mass using Equation

(1) from the ΛCDM simulations in Munari et al. (2013):

$$M_{200} = \left(\frac{\sigma_{1D}}{A_{1D}}\right)^{1/\alpha} \frac{10^{15} M_{\odot}}{h(z)} \qquad (1)$$

with the parameters $A_{1D} = 1090 \pm 50$ and $\alpha = 0.3333$ (see also Evrard et al. 2008). σ_{1D} is the cluster LOS velocity dispersion σ_{disp}, and $h(z) = H(z)/(100 \text{ km s}^{-1})$, where $H(z)$ is the Hubble constant. Assuming virialization, this equation gives the relation between the total mass of a cluster in a radius R_{200}[16] and its velocity dispersion, and is obtained by using a Navarro et al. (1996) dark matter mass profile with different concentration parameters and different constant velocity anisotropies. The uncertainty in the coefficient A_{1D} takes into

---

[16] R_{200} is the radius at which the cluster mean density is 200 times the critical density.

Figure 6. HUDFJ0332.4-2746.6: combined color image of the spectroscopic members, from the ACS B_{435}, WFC3 i_{775} and H_{160} images. Most of the galaxies present spiral morphologies, as expected from most star-forming galaxies. Eight are classified as ETGs (see Table 2). Most show asymmetries, faint substructures and tails, which are signatures of merger remnants. Four galaxies form two confirmed pairs, others have close small companions that are not confirmed to be at the same redshift.

account the uncertainties in these simulation assumptions. From the cluster velocity dispersion we also derive R_{200} (Carlberg et al. 1997).

Following the classic Danese et al. (1980) computation of the intrinsic velocity dispersion, and its uncertainty, we obtain $\sigma_{\rm disp} = 780^{+180}_{-100}\,{\rm km\,s^{-1}}$. This corresponds to a mass of $M_{200} = 2^{+2}_{-1} \times 10^{14}\,M_\odot$, and $R_{200} = 1.0^{+0.3}_{-0.1}$ Mpc.

To take into account possible systematics due to the sample selection, we estimate the uncertainty on the cluster velocity dispersion, its mass, and its virial radius by bootstrapping 1,000 times on the 18 cluster members. Specifically, we recalculated the three quantities, $\sigma_{\rm disp}$, M_{200}, and R_{200}, substituting all the initial sample with a sample of the same size extracted randomly from the initial sample. We obtain an intrinsic velocity dispersion of $\sigma_{\rm disp} = (730 \pm 260)\,{\rm km\,s^{-1}}$, $M_{200} = (2.2 \pm 1.8) \times 10^{14}\,M_\odot$, and $R_{200} = (0.9 \pm 0.3)$ Mpc. This suggests that using the classic computation from Danese et al. (1980) does not take into account all uncertainties in the sample selection, and we will use these last estimates as more robust. If we underestimated systematics on redshift measurements, our mass estimate becomes an upper limit.

When using other values of $A_{\rm 1D}$, obtained using two different models of the baryonic physics in Munari et al. (2013), our results do not significantly change. A systematic of ≈10% in velocity dispersion from the LOS anisotropies would lead to a systematic of ≈10−15% in mass, in this range of velocity dispersion and mass, and does not change our results.

From our conservative result $M_{200} = (2.2 \pm 1.8) \times 10^{14}\,M_\odot$, we can derive a simple quantification for the probability of our hypothesis of virialization. We are consistent with a mass of $M_{200} \geqslant 1 \times 10^{14}\,M_\odot$ at ~75% of probability. If we assume that the structure just started to separate from the Hubble flow (Steidel et al. 1998), we would obtain a mass of the same order of magnitude (≈$10^{14}\,M_\odot$), but with larger systematics due to the difficulty in estimating the three-dimensional volume that the overdensity covers with the available low-resolution

spectroscopy. With the available data, this is the best that we can do.

5. HUDFJ0332.4-2746.6 AND HUDFJ0332.5-2747.3 GALAXY POPULATION
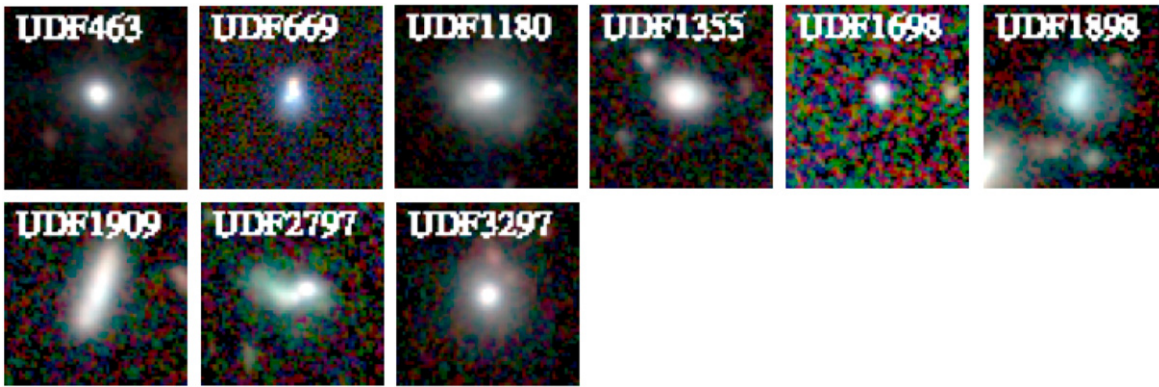
5.1. Morphologies

All of the structures' galaxies but two (see Table 1) show recent star formation. In Figures 6 and 7, we show their color images. Most of the morphologies are disturbed, and often show asymmetry and/or asymmetric tails. Using the WFC3 J_{125} imaging, which corresponds to the B rest-frame at $z = 1.84$-1.9, we visually classified galaxies into two categories: ETGs and late-type galaxies (LTGs). We included compact galaxies in the ETG class, and irregular galaxies in the LTG class. We have seven ETGs at $z = 1.84$, plus UDF-3058 that we consider an ETG with an asymmetric tail, and five ETGs at $z = 1.9$. UDF-1355 looks like an ETG in the B-band rest-frame but shows asymmetric features in the UV. We consider as reliable only the two ETGs brighter than $H_{160} = 23.5$ mag (van der Wel et al. 2012; Kartaltepe et al. 2014). LTGs always reveal structure and are therefore all reliably classified (see also, e.g., Mortlock et al. 2013; Kartaltepe et al. 2014).

Among the candidates at $z = 1.84$, UDF-3058 has an ambiguous morphology, with a bulge-like appearance and an asymmetric tail that appears in the B rest-frame. We classify it as an ETG. One galaxy that we classify as an ETG, UDF 2900, shows a double core in the UV.

For the 17 galaxies with $H_{160} < 24.5$ mag, our classification is consistent with the CANDELS morphological classification from Kartaltepe et al. (2014) for all galaxies. This is a higher than typical level of consistency among different classifiers/classification methods when the morphological classification includes only two broad classes, ETGs and LTGs (e.g., Postman et al. 2005; Huertas-Company et al. 2009, 2010).

Two spectroscopic pairs are close companions, but we do not have enough spectral resolution to identify them as mergers. From Kartaltepe et al. (2014), two objects are

Figure 7. HUDFJ0332.5-2747.3: Combined color image of the spectroscopic members, from the ACS B_{435}, WFC3 i_{775} and H_{160} images. Most of the galaxies present spiral morphologies. Five have early-type morphologies.

classified as mergers ($12^{+13}_{-8}\%$), seven as interacting ($41 \pm 14\%$), six as asymmetric ($35^{+15}_{-13}\%$), four have tidal features ($23^{+14}_{-10}\%$). UDF 3297 has been marked as having a double nucleus. All of this accounts for nine objects ($53^{+14}_{-15}\%$ of the sample), because some objects have multiple features. It is interesting that half of these galaxies are interacting or disturbed, because they show signatures that are characteristic of merger remnants or disk instability (see also results from, e.g., Lotz et al. 2013; Mortlock et al. 2013). The galaxies in these structures are still being assembled and the observation of interactions and disturbed morphologies point to mergers and possibly disk instabilities as the primary mechanisms.

The fraction of confirmed early-type galaxies is at most $48 \pm 10\%$ of the entire sample, against the typical $\approx 80\%$ and close to the $\approx 50-80\%$ observed in galaxy clusters at $z < 1.5$ and $1.5 < z < 2$, respectively, for galaxy masses of $M > 10^{10-10.5} \times M_{\odot}$ and a total cluster mass of $M > 10^{14} \times M_{\odot}$ (e.g., Postman et al. 2005; Desai et al. 2007; Mei et al. 2009, 2012; Tran et al. 2010; Fassbender et al. 2011; Hayashi et al. 2011; Papovich et al. 2012; Tadaki et al. 2012; Zeimann et al. 2012; Brodwin et al. 2013). Our results have to be taken as upper limits to the fractions of ETGs in our structures. In fact, we emphasize that we only consider as secure ETGs those galaxies with $H_{160} < 23.5$ mag, e.g., two over the five ETGs. This means that when calculating the fraction of ETGs, we might be overestimating it, since the three fainter ETGs might not be ETGs.

5.2. Galaxy Masses and Colors

We have used the Guo et al. (2013) photometric catalog to estimate galaxy masses and colors. This catalog includes observations from CANDELS *HST*/WFC3 Y_{105}, J_{125} and H_{160} data, combined with existing public data from the HUDF09 programs. In addition to WFC3 bands, the catalog also includes data from UV (U-band from both CTIO/MOSAIC and VLT/VIMOS), optical (*HST*/ACS F435W, F606W, F775W, F814W, and F850LP), infrared (*HST*/WFC3 F098M, VLT/ISAAC Ks, VLT/HAWK-I Ks), and *Spitzer*/IRAC 3.6, 4.5, 5.8, and 8.0 μm observations (from the GOODS and SEDS surveys: Fazio et al. 2004; Ashby et al. 2013b). We refer to Guo et al. (2013) for a detailed description of these observations. The catalog is based on source detection in H_{160}, and all photometry was matched using the public software TFIT (Laider et al. 2007). The photometry reaches a 5σ depth

(within an aperture of radius $0.''17$) of 29.7 mag in the HUDF region, with a completeness of 50% at 28.1 mag in H_{160}.

We estimated galaxy masses from the Guo et al. broadband photometry, using the public software Le Phare (Arnouts et al. 2002; Ilbert et al. 2006), based on a χ^2 spectral energy distribution fitting method. For our Le Phare input parameters, we followed Ilbert et al. (2010) and used the Chabrier IMF, Bruzual & Charlot (2003) templates, solar metallicity, an exponentially decaying star formation with τ in the range 0.1–5 Gyr, and a Calzetti et al. (2000) extinction law with $E(B-V)$ in the range 0–0.5.

The galaxies in our structures have magnitudes in the range of $22.3 \lesssim J_{125} \lesssim 27.4$ mag and $22 \lesssim H_{160} \lesssim 26.3$ mag ($20.75 \lesssim H_{160}^{\rm VEGA} \lesssim 25$ mag). Their range in luminosity is similar to magnitudes observed in the clusters detected at $z = 1.8\text{-}1.9$ by Stanford et al. (2012) and Zeimann et al. (2012), even if these two clusters' most luminous galaxies are brighter of $\sim 0.5-1$ mag with respect to our most luminous galaxies. This difference of $\sim 0.5-1$ mag is of the same order of magnitude as the difference in luminosity between the most luminous galaxies in different confirmed clusters at $0.8 < z < 1.3$ (Mei et al. 2009).

In Figure 8, we show the color–magnitude and color-mass relations. All galaxies have masses in the range of $8.9 \lesssim \log_{10}\left(\frac{M}{M_{\odot}}\right) \lesssim 10.8$, and all of their colors, but one (UDF-463), which also does not show emission lines, are bluer than quiescent galaxies at these redshifts. In fact, at z=1.84 and according to a Bruzual & Charlot (2003) simple, single starburst model with solar metallicity, we would expect a red sequence at $(I_{814} - J_{125}) \approx 2.3$ mag, for a formation redshift $z_f = 2.5$. This value corresponds to the mean luminosity-weighted formation redshift usually derived for galaxies in clusters at $z \approx 1-1.5$ (e.g., Mei et al. 2006a, 2006b, 2009, 2012; Snyder et al. 2012; Brodwin et al. 2013; and references therein). We show as a continuous line the color–magnitude relation at $z \sim 1$ from Mei et al. (2009) passively evolved to $z = 1.84$. The dashed lines show three times their total observed scatter ($3 \times \sigma_{\rm obs} \sim 0.2$). Hereafter, we define as *red* galaxies those that are redder than the passively evolved red sequence minus $3 \times \sigma_{\rm obs}$. It is clear that most of the ETGs in these structures still need to be quenched.

Unlike the known clusters at $z \approx 1.8-2$ (Stanford et al. 2012; Zeimann et al. 2012; Newman et al. 2014; Gobat et al. 2011, 2013) that show overdensities of $\sim 10-15$ red galaxies, the two overdensities do not show an already formed
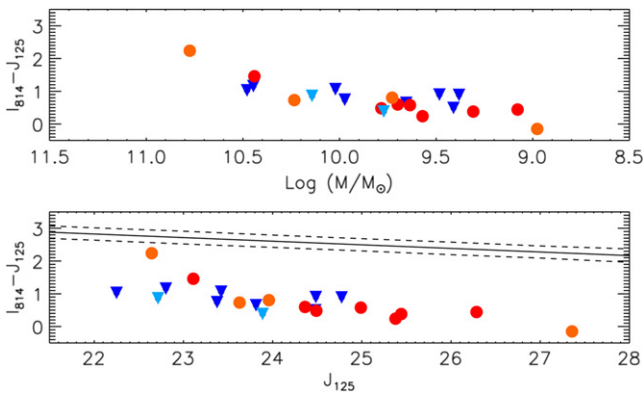
Figure 8. Color–magnitude and color-mass diagram for all HUDFJ0332.4-2746.6 and HUDFJ0332.5-2747.3 spectroscopically confirmed members with Guo et al. (2013) photometry. The selected galaxies have masses in the range $8.9 < \log_{10}\left(\frac{M}{M_\odot}\right) < 11$. The $(I_{814} - J_{125})$ color is close to the $(U - B)$ rest-frame, and J_{125} to the B-band rest-frame. Red/orange circles and blue/sky triangles are ETGs and LTGs in HUDFJ0332.4-2746.6/HUDFJ0332.5-2747.3, respectively. We show as a continuous line the color–magnitude relation at $z \sim 1$ from Mei et al. (2009) passively evolved at $z = 1.84$, and the dashed lines show a region within three times the observed scatter. A red sequence is not yet formed.

red sequence. Only one of the structure galaxies has a color red enough to be considered as a red sequence galaxy at these redshifts.

Potential red sequence galaxies could have been missed in our spectroscopical analysis because we only selected star-forming galaxies, or only those with good quality spectra from the 3D-*HST*, CANDELS, and GMASS catalogs. However, when using the entire Guo et al. photometric catalog in the HUDF, there are only six other red galaxies (e.g., as defined above, with $(I_{814} - J_{125}) > 1.7$ mag) within 1.′5 from the proto-cluster and group centers from the spectroscopic redshift catalog from GMASS, the photometric and photometric redshift catalog (used without any selection in redshift) from Guo et al. (2013), the CANDELS morphology catalog from Kartaltepe et al. (2014), which we have examined one by one using the Guo et al. (2013) photometry. The three brightest of the six red galaxies are within 1′ from the proto-cluster, have spectroscopic redshift measurements that are at lower or at higher redshift, and do not belong to the two overdensities.

We robustly confirm that HUDFJ0332.4-2746.6 and HUDFJ0332.5-2747.3 do not have an already formed red sequence, within 1.5′ of the proto-cluster and group centers.

We also examined the colors of the photometric redshift overdensities around HUDFJ0332.4-2746.6 and HUDFJ0332.5-2747.3. In Figures 4 and 5, Group 1, Group 2, Group 4, and Group 6 have promising bright red sequences. Using the spectroscopic redshift catalog available in the GOODS area (Wuyts et al. 2008, 2009; J. Kurk et al. 2015, in preparation) the red sequence galaxies with known redshifts (a circle surrounds their symbols in Figures 4 and 5) do not show spectroscopic redshifts in the the range of HUDFJ0332.4-2746.6 and HUDFJ0332.5-2747.3. In the figures, we also show AGN detections from Xue et al. (2011). Group 1 has two red galaxies with spectroscopic redshifts, with $z = 2.35$ and $z = 1.76$. Group 6 has three red galaxies with spectroscopic redshifts, two also belonging to Group 1 and one at higher redshift.

5.3. Galaxy Structural Properties

As demonstrated by van der Wel et al. (2012), the WFPC3/IR camera resolution together with the depth of CANDELS observations, permit us to estimate galaxy structural parameters up to $H_{160} \approx 23$ mag, and galaxy sizes up to $H_{160} \approx 24.5$ mag. Bassett et al. (2013) have also shown that the same applies up to $J_{125} = 24$ mag.

We estimated galaxy structural parameters for all galaxies (ETGs and LTGs) using GALFIT (Peng et al. 2002, 2010) on the WFC3/IR J_{125} image from XUDF, that corresponds to the B-band rest-frame at $z \sim 1.8-1.9$. We have adopted a single Sérsic profile, and did not constrain the values of the Sérsic index n for most of the sample, as suggested in Peng et al. (2002). The point-spread function (PSF) model was provided by van der Wel et al. (2012). The galaxies classified as late-type all have a Sérsic index of $n < 2$, the two bright ETGs have $n > 2$ and the other ETGs have $1 < n < 2$. As the size estimate, we use the circularized effective radius R_e, defined as the average half-light-radius along the major axis of the best-fitting galaxy model multiplied by the ratio between the minor and major axis $q = \sqrt{b/a}$.

Figure 9 shows the galaxy mass–size relation. The two stars show the ETG mass–size relation observed in galaxy clusters at a redshift of $1.2 < z < 1.5$ from Delaye et al. (2014), and the dark blue circles show results from Lani et al. (2013) ($1 < z < 2$), for their most dense regions (see also Papovich et al. 2012; Bassett et al. 2013).

These previous works pointed out that ETGs in clusters have, on average, larger sizes than ETGs in the field at the same redshift (within $\sim 2\sigma$), when the mass–size relation is taken into account (see also Cooper et al. 2012; Raichoor et al. 2012; Newman et al. 2014). For clusters in the same redshift range that our structures, the filled square and diamonds, are the ETG masses and circularized effective radii from CL J1449+085 at $z \sim 2$ (Strazzullo et al. 2013) and JKCS 041 at $z = 1.8$ (Newman et al. 2014), respectively, with masses corrected to a Chabrier IMF. All sizes are measured in the B-band rest-frame. Our structures' ETGs all have masses of $M < 10^{11}\,M_\odot$, in the same range of the masses of passive ETGs in CL J1449 +085 (see the filled squares), and are about an order of magnitude lower than the most massive ETGs in the most massive cluster known at these redshifts, JKCS 041 (see the filled diamonds).

As a reference, we show the SDSS mass–size relation for ETG and LTG galaxies from Bernardi et al. (2012). While the Bernardi et al. mass–size relation has been estimated for field galaxies, it also holds for galaxy cluster for the ETGs (Huertas-Company et al. 2013b), and we do not expect large variations for the LTGs (Fernández-Lorenzo et al. 2013). Our structures' LTGs lie on the same mass–size relation as Bernardi et al. (2012) LTGs. For the ETGs, assuming that the form of the mass–size relation from Bernardi et al. (2012) does not evolve with redshift, when extrapolating the Delaye et al. (2014) and Lani et al. (2013) mass–size relations at lower masses, our structures' ETGs follow the same mass–size relation at $1 < z < 2$.

It is very interesting, because this is also true for the ETGs in JKCS 041 and CL J1449+085. To better quantify this point, in Figure 10, we plot the mass-normalized B-band rest-frame size, γ, as a function of redshift, for passive ETGs in clusters at $0.7 < z < 1.6$ from Delaye et al. (2014), JKCS 041 at $z = 1.8$ (from Newman et al. 2014) and CL J1449+085 at $z \sim 2$ (from
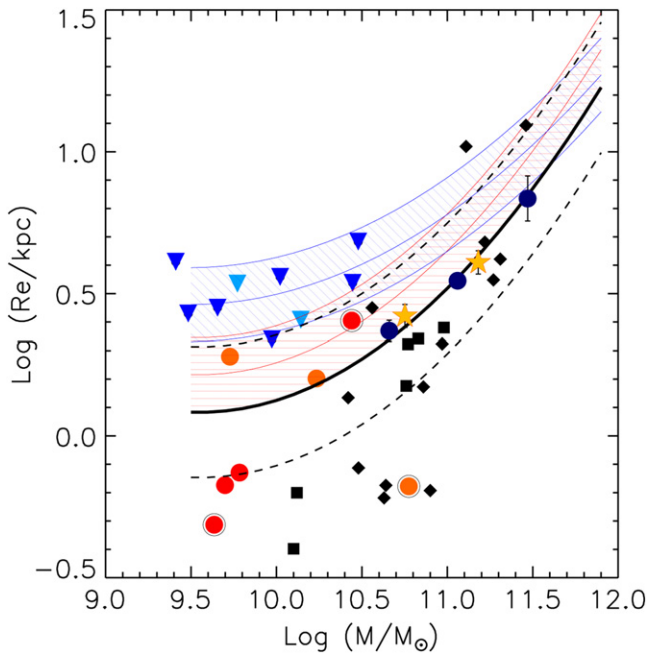
Figure 9. Mass–size relation for galaxies with $H_{160} > 24.5$ mag in HUDFJ0332.4-2746.6 and HUDFJ0332.5-2747.3. Red/orange circles and blue/sky triangles are ETGs and LTGs in HUDFJ0332.4-2746.6/ HUDFJ0332.5-2747.3, respectively. The black circles around filled symbols show galaxies with $n > 2$. The two stars show the ETG mass–size relation observed in galaxy clusters at a redshift of $1.2 < z < 1.5$ from Delaye et al. (2014), and the dark blue circles show results from Lani et al. (2013) ($1 < z < 2$), for their most dense regions. The filled squares and diamonds are the quiescent ETG masses and circularized effective radii from CL J1449+085 at $z = 1.99$ (from Strazzullo et al. 2013) and JKCS 041 at $z = 1.8$ (from Newman et al. 2014), respectively. All ETGs from CL J1449+085 and JKCS 041 have been selected as galaxies with $n > 2$. As a reference, we show the SDSS local mass–size relation from Bernardi et al. (2012). The red/blue continuous line shows the mass–size relation for SDSS ETG/LTG, respectively. The shaded regions show the 1σ observed scatter. The continuous black line is the local mass–size relation scaled to the average sizes from Delaye et al. at $10^{11} M_\odot$ (the dashed lines indicate the observed scatter). Our blue star-forming ETGs lie on the same mass–size relation as quiescent ETGs in dense environments at $1 < z < 2$.

Strazzullo et al. 2013), and the star-forming ETGs in HUDFJ0332.4-2746.6 from this work. Since our galaxies span a large range in mass ($10^{9.5} M_\odot \lesssim M \lesssim 10^{12} M_\odot$, we calculate γ using the SDSS mass–size relation in Bernardi et al. (2012); Equation (1)), instead of the commonly used power law that holds for galaxy masses $M > 10^{11} M_\odot$:

$$\log(\gamma) = \log(R_e) + c1 \times \left[\log\left(\frac{M}{10^{11} M_\odot} \right) \right] + c2$$

$$\times \left\{ [\log(M)]^2 - \left[\log\left(10^{11} M_\odot \right) \right]^2 \right\}, \qquad (2)$$

where R_e and M are the galaxy circularized effective radius and mass in units of $M_\odot$, respectively, and $10^{11} M_\odot$ is the typical mass used for the mass normalization. $c1$ and $c2$ are the coefficients for ETGs and LTGs from Bernardi et al. (2012). The uncertainties have all been estimated by bootstrap with replacement, with 1000 iterations. Both the quiescent and the star-forming ETG median normalized sizes do not evolve significantly from $z \sim 2$ to $z \sim 0.7$ (~20%). When using the average γ instead of the median, results are consistent. This
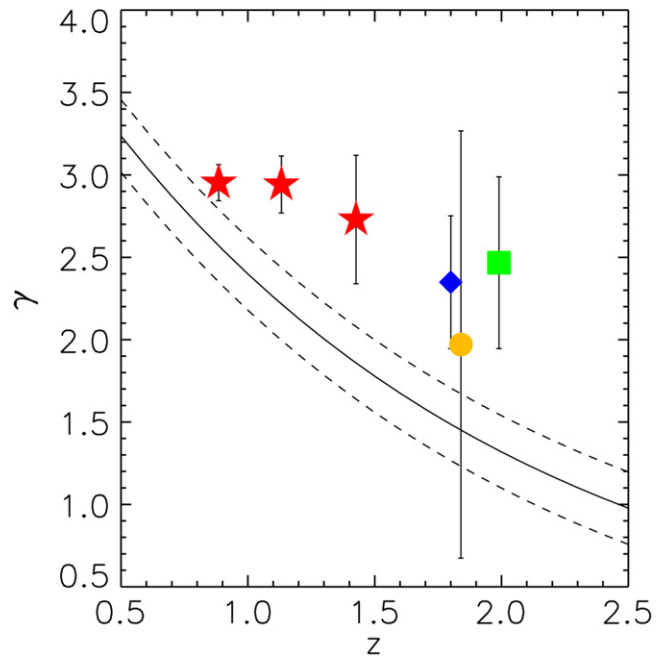
Figure 10. Median mass-normalized B-band rest-frame size γ, as a function of redshift. The yellow circle is the median γ for HUDFJ0332.4-2746.6 ETGs. The red stars are the median γs for quiescent ETGs in clusters at $0.7 < z < 1.6$ from Delaye et al. (2014). The green square and the blue diamond are the median γs for quiescent ETGs from CL J1449+085 at $z = 1.99$ (Strazzullo et al. 2013) and JKCS 041 at $z = 1.8$ (Newman et al. 2014), respectively. Our structures' star-forming blue ETGs are consistent with those of quiescent ETGs in dense environments at similar redshifts. Both star-forming and quiescent ETGs in dense environments do not show much evolution in the redshift range of $z = 0.7-2$. The continuos line shows the evolution of field galaxies and is from Newman et al. (2012).

redshift range corresponds to a time interval of ~4 Gyr, over which ETG sizes must have evolved on average according to the same mass–size relation as that of cluster ETGs at $z \sim 1$.

On the low-mass-end side ($M < 10^{11} M_\odot$), our structures's ETGs must have had their star formation quenched, though, to be selected as passive ETGs in the $z \approx 1$ samples.

In Table 2, we give the galaxy magnitudes, colors, masses, and structural parameters.

6. DISCUSSION AND CONCLUSIONS

Deep mid-infrared surveys, and space and ground-based infrared spectroscopy have enabled the discovery of clusters of galaxies at redshift $z = 1.5-2$, an epoch largely unexplored until recently. Most of these discoveries have been based on the searches for star-forming galaxy overdensities around radio sources, and/or red galaxy overdensities in the mid-infrared with *Spitzer* IRAC. The advent of the *HST* WFC3 grism and ground-based infrared spectroscopy permits confirmation of these discoveries as real galaxy overdensities (Stanford et al. 2012; Zeimann et al. 2012; Gobat et al. 2013; Newman et al. 2014).

Current X-ray and SZ observations probe cluster virialization through the detection of the hot gas in the gravitational potential well, down to cluster masses of $\approx 10^{14} M_\odot$ and up to redshift $z \approx 1$. At higher redshifts, only the extreme end of the cluster mass function can be detected by current instruments. A few objects at $1.5 < z < 2$ correspond to significant X-ray detections and were identified as already virialized (Andreon et al. 2009;

Gobat et al. 2011; Santos et al. 2011; Stanford et al. 2012; Mantz et al. 2014). Two of them also show a significant SZ signal (Brodwin et al. 2012; Mantz et al. 2014). Their cluster masses cover the range of $M_{200} \approx (0.5 - 4) \times 10^{14} M_{\odot}$. The other detections (e.g., less massive objects) can only currently be identified as significant red galaxy overdensities, without confirmation of virialization by the detection of hot gas. Depending on the presence, or not, of the red sequence and their richness, these objects have been identified as clusters or proto-clusters (e.g., Pentericci et al. 2000; Miley et al. 2004, 2006; Venemans 2007; Kuiper et al. 2010; Hatch et al. 2011).

In this paper, we presented the discovery of two star-forming galaxy overdensities in the HUDF using *HST* WFC3 grism spectroscopy and imaging observations from the CANDELS and 3D-*HST* Treasury programs. The richest overdensity, HUDFJ0332.4-2746.6, includes 18 spectroscopic members, of which 6 are ETGs. The other one, HUDFJ0332.5-2747.3, includes 7 spectroscopic members, of which 3 are ETGs. Our detections are mostly based on line emitter galaxy over-densities, similar to current proto-cluster discoveries at $z > 2$, but different from current cluster detections at the same redshift that are based on red galaxy overdensities. We confirmed the grism redshifts using deep far-UV photometry from the UVUDF (Teplitz et al. 2013).

Using an *N*th-nearest neighbor distance estimator and the density contrast, we measure a galaxy overdensity at $\sim20\sigma$ and $\sim(4-7)\sigma$ above the background, for HUDFJ0332.4-2746.6 and HUDFJ0332.5-2747.3, respectively. Under the hypothesis of virialization, from HUDFJ0332.4-2746.6 velocity dispersion, we obtain a mass estimate of $M_{200} = (2.2 \pm 1.8) \times 10^{14} M_{\odot}$, consistent with the lack of extended X-ray emission. In Table 3, we compare our newly discovered structure to already known clusters, proto-clusters, and groups at $z = 1.6-2$. Within the uncertainties, HUDFJ0332.4-2746.6 has the properties char-acteristic of a proto-cluster, because of its overdensity and estimated mass, and HUDFJ0332.5-2747.3 those of a galaxy group, because of its overdensity.

Predictions from numerical simulations (Cohn & White 2005; Li et al. 2007; Chiang et al. 2013; Cautun et al. 2014) suggest that HUDFJ0332.4-2746.6 is most probably a progenitor of $M_{200} \approx 10^{14} M_{\odot}$ galaxy clusters at $z \sim 1$ and of $M_{200} \approx$ few $\times 10^{14} M_{\odot}$ galaxy clusters at the present. At $z \approx 1.8-1.9$ Chiang et al. (2013) predict the comoving effective sizes of clusters of mass $M_{200} \approx 10^{14} M_{\odot}$ to be $\approx2-5$ Mpc. Their total mass extends beyond this spatial scale, based on the cosmological N-body simulation from the Millennium Run (Springel et al. 2005) and semi-analytic galaxy catalogs from Guo et al. (2011). Within the GOODS-CDFS area covered by the Guo et al. (2013) photometric redshift catalog, we searched for overdensities in photometric redshift ranges around the two overdensities and found several groups. Without extensive spectroscopic follow-up we cannot conclude that these groups are at the same spectroscopic redshift as our newly discovered structures. It would be interesting to follow them up spectroscopically and understand if our two overdensities are part of a larger structure at the same redshift.

We estimate that at most $\approx50\%$ of the proto-cluster members are ETGs, against the 80% observed in clusters of galaxies at $z \approx 1-1.5$ (e.g., Postman et al. 2005; Mei et al. 2009, 2012). About 50% of the structure members show possible

interactions or disturbed morphologies (asymmetries, faint substructures, and tails), which are possible signatures of merger remnants or disk instability. This suggests mergers and possibly disk instabilities as the primary and ongoing mechanisms of assembly in at least half of the galaxies in dense environments at these redshifts.

For galaxy clusters and proto-clusters at $z = 1.6-1.9$, the ETG fractions can be quite different in different objects, going from 50% (Gobat 2013; Zeimann et al. 2012; Muzzin et al. 2013) to 80% (Papovich et al. 2012). The lower end of these estimated fractions and our results are close to the fractions of ETGs with masses of $M > 10^{10} M_{\odot}$ obtained from Mortlock et al. (2013) in the CANDELS Ultra-deep Survey. This suggests the existence of significant overdensities that have similar ETG fractions as the field. It is also interesting that Mortlock et al. found that $z \sim 1.85$ is a redshift of transition between an epoch in which irregular galaxy fractions dominate over disk galaxy fractions to an epoch in which the trend is inverted to the type fractions observed in the local universe.

Using multi-wavelength photometry from Guo et al. (2013), we study the two structures' galaxy colors, and find that their red sequence is not yet in place. All the confirmed ETG members, but two, show emission lines that indicate recent star formation activity. Only one ETG shows colors consistent with those characteristic of an old stellar population at these redshifts, e.g., all the others have active stellar populations. This is consistent with the fact that most of the ETGs in the two structures are star-forming and will be quenched only at a later time.

From both of the two structures' ETG fractions and their colors, new ETGs would need to be formed (e.g., by transformations of LTGs by environmental effects; e.g., Boselli & Gavazzi 2006) or accreted, to obtain the higher ETG fractions observed at lower redshifts. The progenitors of some of these newly transformed ETGs could have been observed as a passive bulge-dominated LTG population in clusters and dense regions at $z = 1-1.3$ (Mei et al. 2006a, 2006b, 2012; Bundy et al. 2010; George et al. 2013).

Current red sequence galaxies are predicted to form the bulk of their stars at an average formation redshift of $z_f = 2-3$ from both the interpretation of their scaling relations and age and metallicity measurements (e.g., Thomas et al. 2005), and semianalytic models based on the Millennium simulation (e.g., de Lucia & Blaizot 2007; Barro et al. 2014; Shankar et al. 2013). This implies that part of their progenitors at $z \approx 2$ are star-forming galaxies. Combined deep high resolu-tion space imaging and grism spectroscopy permitted us to spectroscopically confirm star-forming blue ETG progenitors. At least part of the red sequence ETGs are already ETGs and are compact before quenching their star formation. Our results are consistent with recent observations in the HUDF and modeling by Barro et al. (2013, 2014) that demonstrated how compact star-forming galaxies (all morphology selected) appear to be progressively quenched from $z = 2-3$ to $z = 1-2$. In this work, we spectroscopically confirm for the first time the presence of star-forming blue compact ETGs in significant galaxy overdensities, e.g., in a proto-cluster. Since star-forming ETGs are rare both in clusters and the field up to $z \approx 1.5$ (e.g., Mei et al. 2009; Huertas-Company et al. 2010; Barro et al. 2013a, 2013b; Brodwin et al. 2013, and references therein), the star-forming ETGs are most probably (at least part of) the progenitors of passive ETGs in galaxy clusters at $z \sim 1-1.5$.

Table 2
Spectroscopic Members for HUDFJ0332.4-2746.6 and HUDFJ0332.5-2747.3

ID	R.A. (J2000)	Decl.(J2000)	z	H_{160} (mag)	$(I_{814} - J_{125})$(mag)	Morphology	Spectral Features (Q)	$\mathrm{Log}_{10}(M/M_\odot)$	$R_e \times \sqrt{b/a}$ (kpc)	N_{Sersic}
HUDFJ0332.4-2746.6										
UDF-901	53.15126	−27.79241	1.841 ± 0.001	23.970 ± 0.005	0.597 ± 0.042	ETG	O III, Hβ ,Hγ	9.7	0.67 ± 0.01	1.85 ± 0.04
UDF-1271/GMASS-675	53.16166	−27.78743	1.836 ± 0.008	22.475 ± 0.002	1.158 ± 0.027	LTG	*O III, Hβ*(3.3)	10.5	3.45 ± 0.01	0.47 ± 0.01
UDF-2090	53.15346	−27.78098	1.849 ± 0.001	24.489 ± 0.008	0.576 ± 0.071	ETG	O III, Hγ	9.6	0.49 ± 0.07	10 ± 2
UDF-2095/GMASS-858	53.15565	−27.77930	1.839 ± 0.003	22.008 ± 0.002	1.029 ± 0.019	LTG	O III, Hβ, Hγ (8.4)	10.5	4.82 ± 0.04	1.15 ± 0.01
UDF-2103	53.15351	−27.78091	1.838 ± 0.004	⋯	0.576 ± 0.071	ETG	O III			
UDF-2127	53.15287	−27.78012	1.858 ± 0.003	24.292 ± 0.008	0.899 ± 0.068	LTG	O III	9.5	2.69 ± 0.04	1.46 ± 0.02
UDF-2188/ GMASS-875	53.15452	−27.77972	1.836 ± 0.004	23.624 ± 0.005	0.649 ± 0.035	LTG	O III (5.1)	9.7	2.82 ± 0.02	0.43 ± 0.01
UDF-2195/GMASS-894	53.14921	−27.77880	1.850 ± 0.002	23.189 ± 0.004	1.064 ± 0.038	LTG	O III, *O III*x, Hβ, Hδ (4.6)	10.0	3.62 ± 0.01	0.27 ± 0.01
UDF-2383	53.14642	−27.77831	1.865 ± 0.001	24.701 ± 0.009	0.239 ± 0.067	ETG	O III	⋯	⋯	⋯
UDF-2433	53.14744	−27.77761	1.825 ± 0.002	22.708 ± 0.003	1.459 ± 0.056	ETG	O III, *O III*x	10.4	2.5 ± 0.1	6.8 ± 0.1
UDF-2491	53.14744	−27.77761	1.889 ± 0.007	⋯	1.459 ± 0.056	LTG	O III			
UDF-2798	53.13924	−27.77485	1.843 ± 0.002	25.689 ± 0.051	0.442 ± 0.115	ETG	O II, O III	⋯	⋯	⋯
UDF-2900	53.15288	−27.77250	1.845 ± 0.001	24.019 ± 0.005	0.481 ± 0.043	ETG	O III, Hβ, Hγ	9.8	0.74 ± 0.01	1.33 ± 0.03
UDF-3035[a]	53.15605	−27.77095	1.833 ± 0.004	24.587 ± 0.009	0.889 ± 0.085	LTG	*O II, O III, Hγ*			
UDF-3045	53.15228	−27.77009	1.848 ± 0.001	23.144 ± 0.003	0.743 ± 0.029	LTG	O III, Hβ, Hγ	10.0	2.18 ± 0.01	1.53 ± 0.04
UDF-3058	53.16001	−27.77100	1.853 ± 0.002	25.223 ± 0.012	0.381 ± 0.072	ETG	O III	⋯	⋯	⋯
UDF-3510	53.16387	−27.76532	1.841 ± 0.003	24.241 ± 0.007	0.494 ± 0.046	LTG	O III, Hβ, Hγ	9.4	4.10 ± 0.05	0.79 ± 0.01
GMASS220	53.15492	−27.80940	1.850 ± 0.001	⋯	⋯	LTG	Fe, C (4.7)	⋯	⋯	⋯
HUDFJ0332.5-2747.3										
UDF-463	53.15881	−27.79716	1.904 ± 0.004	24.292 ± 0.008	2.239 ± 0.062	ETG	4000 Å break	10.8	0.66 ± 0.01	2.49 ± 0.02
UDF-669	53.14060	−27.79562	1.909 ± 0.002	23.970 ± 0.005	0.730 ± 0.029	ETG	O III, Hβ, Hδ	10.8	0.66 ± 0.01	2.49 ± 0.02
UDF-1180	53.14930	−27.78853	1.907 ± 0.002	22.464 ± 0.002	0.862 ± 0.020	LTG	O III, O II, Hβ, *O III*x, Hδ	10.1	2.56 ± 0.02	1.42 ± 0.01
UDF-1355	53.14799	−27.78769	1.884 ± 0.006	22.475 ± 0.002	0.805 ± 0.038	ETG	O III (4.4)	9.7	1.90 ± 0.01	0.69 ± 0.01
UDF-1698	53.16935	−27.78499	1.911 ± 0.002	24.701 ± 0.009	-0.150 ± 0.196	ETG	O III	⋯	⋯	⋯
UDF-1898[a]	53.17368	−27.78207	1.894 ± 0.058	22.708 ± 0.003	2.140 ± 0.228	LTG	*O III*x, *Hβ*	⋯	⋯	⋯
UDF-1909[a]	53.14903	−27.78196	1.917 ± 0.017	24.489 ± 0.008	1.050 ± 0.041	LTG	*O III, Hδ*	⋯	⋯	⋯
UDF-2797	53.14418	−27.77356	1.892 ± 0.001	23.624 ± 0.005	0.385 ± 0.027	LTG	O III, Hβ, Hδ, Hγ	9.8	0.74 ± 0.01	0.37 ± 0.01
UDF-3297	53.14102	−27.76673	1.904 ± 0.006	23.189 ± 0.004	2.246 ± 0.036	ETG	4000 Å break	⋯	⋯	⋯

Note. Galaxies are identified by their 3D-*HST* ID (UDF; from Brammer et al. 2012) or GMASS ID (GMASS; from Kurk et al. 2013). Redshifts and uncertainties for GMASS are from Kurk et al. (2013). Magnitudes and colors are from Guo et al. (2013). The two galaxy pairs are not separate in this catalog, and we give the magnitude of the Guo et al. object for one of the two galaxies. For the spectral features, O III and O III*x* indicate the [O III]λ5007 and the [O III]λ4363 emission lines, respectively, Hβ the [Hβ]λ4861 emission line, Hγ the [Hγ]λ4340, and O II the [O II]λ3727. The lines are in italics if they were measured with a $1 < S/N < 3$, otherwise they were measured with $S/N > 3$. When the galaxies also have a GMASS redshift, in parenthesis is given the GMASS redshift S/N. The flag (a) means all lines were measured with $S/N < 1$. Galaxies with IDs in italic are not considered as structure members because they have low S/N spectroscopy, and are not detected in the 336*W* bandpass. We estimated structural properties for all galaxies with $H_{160} < 24.5$ mag, where the J_{125} images were available. Statistical uncertainties on masses are a few dex, while systematics, due to the use of different spectral energy distribution templates are <0.5 dex (e.g., Delaye et al. 2014). The uncertainties on galaxy sizes and the Sérsic index are the fit uncertainties given by GALFIT. The typical systematic uncertainties on Re, $\sqrt{b/a}$ and Sérsic index at these magnitudes are ∼20% up to $H_{160} = 24.5$ mag (e.g., van der Wel et al. 2012; Bassett et al. 2013).

Table 3
Comparison of HUDFJ0332.4-2746.6 and HUDFJ0332.5-2747.3 Properties with Those of Already Known Clusters, Proto-clusters, and Groups at $z = 1.6-2$

Name	Identification	z	Overdensity	σ_{disp} (km/s)	Mass ($10^{14} \times M_\odot$)	X-ray Lum./Detection (10^{43} erg s^{-1})	Reference
CL J033211.67-274633.8	Group	1.61	$\sim 5\sigma$	⋯	$M_{200}^{(a)} = 0.32 \pm 0.08$	1.8 ± 0.6	Tanaka et al.
IRC-0218A/ XMM-LSS J02182-05102	Proto-cluster	1.62	$>20\sigma$	860 ± 490	$M_{200}^{(b)} \sim 0.1-0.4$	$>4\sigma$ Detection	Papovich et al. 2010, 2012
SpARCS J022427-032354	Cluster	1.63	⋯	⋯	⋯	Detection	Muzzin et al. (2013)
IDCS J1426+3508	Cluster	1.75	⋯	⋯	$M_{200}^{(a)} \sim 5.6 \pm 1.6$	55 ± 12	Stanford et al. 2012; Brodwin et al. 2012
JKCS 041	Cluster	1.80	⋯	⋯	$M_{200}^{(c)} \sim 2$	76 ± 5	Newman et al. 2014; Andreon et al. 2013
HUDFJ0332.4-2746.6	Proto-cluster	1.84	$\sim 20\sigma$	730 ± 260	$M_{200}^{(b)} = 2.2 \pm 1.8$	$<1-6$	This work
IDCS J1433.2+3306	Cluster	1.89	⋯	⋯	$M_{200} \sim 1$	⋯	Zeimann et al. 2012
HUDFJ0332.5-2747.3	Group	1.90	$\sim 4-7\sigma$	⋯	⋯	⋯	This work
CL J1449+085	Cluster	1.99	$>20\sigma$	⋯	$M_{200}^{(a)} = 0.53 \pm 0.09$	6.4 ± 1.8	Gobat et al. 2013

Note. All estimates are given as they are from the references. For the overdensities, σ is estimated with respect to the background, as given by the references. X-ray fluxes and mass estimates have not been homogenized. (a) and (b) indicate mass estimates derived from the X-ray flux and the velocity dispersion, respectively. (c) indicates that the mass estimate is derived from the X-ray flux and cluster richness.

We compare the masses and the sizes of the structures' star-forming blue ETGs with those of passive ETGs in dense regions and galaxy clusters at $z = 1-2$, and find that they lie on the same mass–size relation. Interestingly, quiescent ETGs in galaxy clusters at $z = 1.8 = 2$ show a similar behavior as our structurer's blue star-forming ETGs, and the mass-normalized B-band rest-frame size, γ, does not significantly evolve in the redshift range $0.7 < z < 2$, contrary to field ETGs (Damjanov et al. 2011; Cimatti et al. 2012; Newman et al. 2014). This implies that, if these objects are the progenitors of quiescent ETGs in clusters at $z = 1-1.5$, their mass-size relation did not evolve significantly even if their star formation was quenched; galaxies could increase their mass, simultaneously increasing their size according to this relation.

The diversity of these structures shows how overdensities at $z > 1.5$ have less homogeneous galaxy populations than those at $z < 1.5$. Large studies of clusters and proto-clusters at these higher redshift have to quantify how detection techniques impact their sample selection function, to obtain good statistics of their galaxy population.

7. SUMMARY

We found star-forming blue ETGs in two newly discovered galaxy overdensities at $z = 1.84$ and $z = 1.9$ in the HUDF. We summarize our main results here.

1. We discovered two galaxy overdensities in the HUDF. The first is identified as a galaxy proto-cluster at $z = 1.84 \pm 0.01$, HUDFJ0332.4-2746.6, and includes 18 spectroscopic members, for a galaxy overdensity of $\sim 20\sigma$. The second is a galaxy group at $z = 1.90 \pm 0.01$, HUDFJ0332.5-2747.3, with seven spectroscopic members, and a galaxy overdensity of $\sim 4-7\sigma$. Under the hypothesis of virialization, from its velocity dispersion, we obtain a mass estimate for HUDFJ0332.4-2746.6 of $M_{200} = (2.2 \pm 1.8) \times 10^{14} M_\odot$, consistent with the lack of extended X-ray emission.

2. The two structures have not yet formed a red sequence. For the first time, we confirm a significant presence of star-forming blue ETGs in dense environments at $z \sim 1.8-1.9$. We classified eight and five ETGs in HUDFJ0332.4-2746.6 and HUDFJ0332.5-2747.3,

respectively, of which five have $J_{125} < 24.5$ mag. The ETG fraction in both structures is at most $\sim 50\%$, similar to fractions obtained in some galaxy clusters (Gobat 2013; Zeimann et al. 2012; Muzzin et al. 2013) and close to those obtained in the field at these redshifts (Mortlock et al. 2013). These are lower fractions than what is observed in some other galaxy clusters at similar redshifts (Papovich et al. 2012) and in galaxy clusters at $z < 1.5$ (80%; e.g., Postman et al. 2005; Desai et al. 2007; Mei et al. 2009, 2012). This suggests that large overdensities at $z > 1.5$ have more diverse galaxy populations than those at $z < 1.5$, and that it is essential to quantify how detection techniques impact our cluster/proto-cluster selection function.

3. About 50% of the structure members show possible interactions or disturbed morphologies, with asymmetries, faint substructures, and tails, all possible signatures of merger remnants or disk instabilities. This suggests mergers and possibly disk instabilities as the primary and ongoing mechanisms of assembly in at least half of the galaxies in dense environments at these redshifts.

4. The star-forming blue ETG have masses of $8.9 \lesssim \log_{10}\left(\frac{M}{M_\odot}\right) \lesssim 10.8$, and their mass–size relation lies on the same mass–size relation observed for quiescent ETGs in clusters and dense regions at $z = 0.7-2$ (Lani et al. 2013; Newman et al. 2014; Strazzullo et al. 2013; Delaye et al. 2014). Interestingly, quiescent ETG sizes in clusters also do not evolve significantly in this redshift range, which covers ~ 4 Gyr in time. This suggest that at these epochs, cluster ETGs do not significantly change their median/average sizes, and evolve according to a mass–size relation similar to the one at $z \sim 1$.

5. Both of the two structures' ETG fractions and their colors suggest that these star-forming blue ETGs are the most likely progenitors of at least part of the passive ETGs observed in clusters at $z < 1$. Their masses are $\sim 3-5$ times lower than the most massive ETGs in these lower redshift clusters. More (massive) ETGs have to be formed/accreted and then quenched, to obtain the ETG fractions, colors, and masses observed in clusters at $z < 1$.
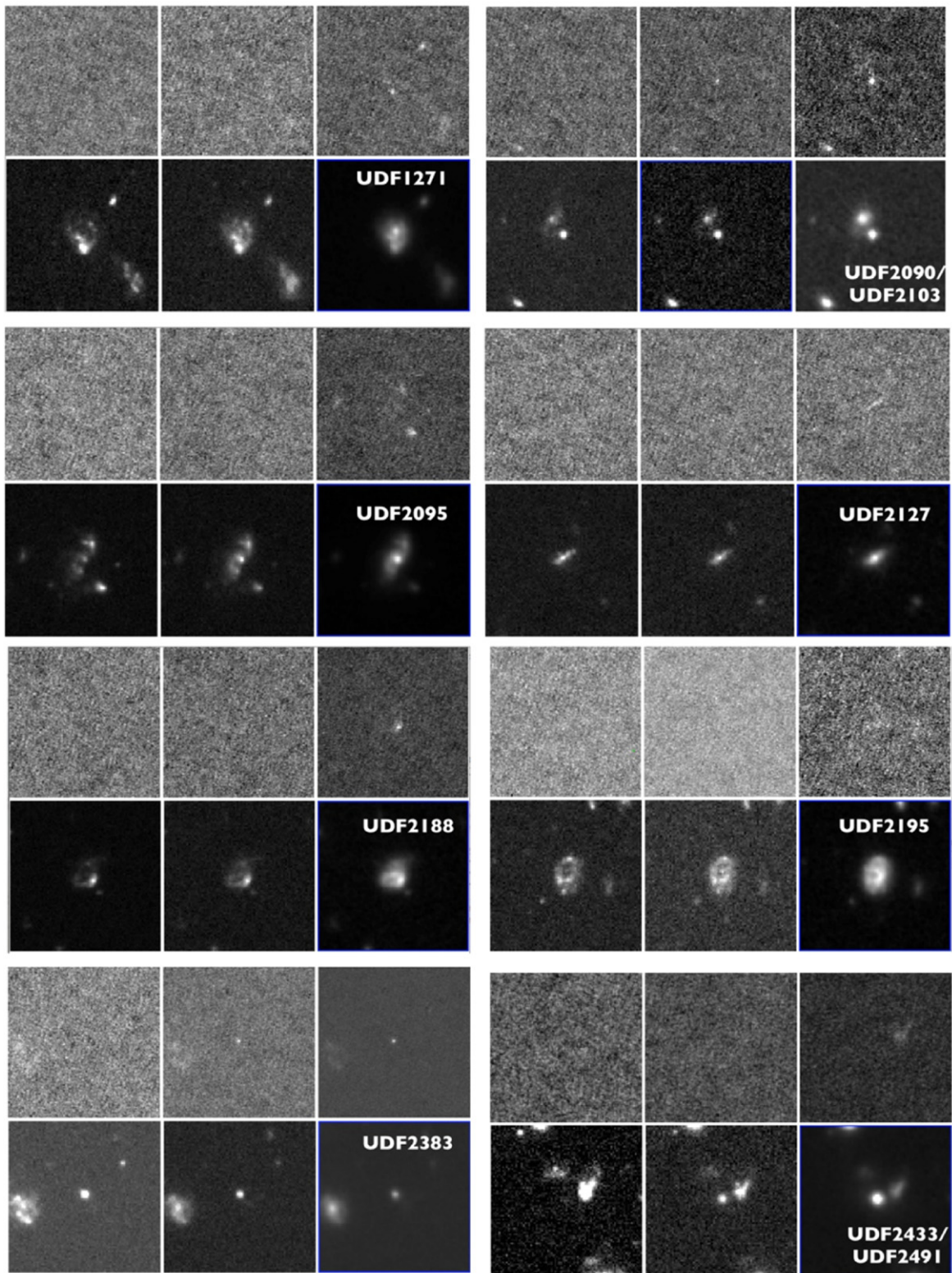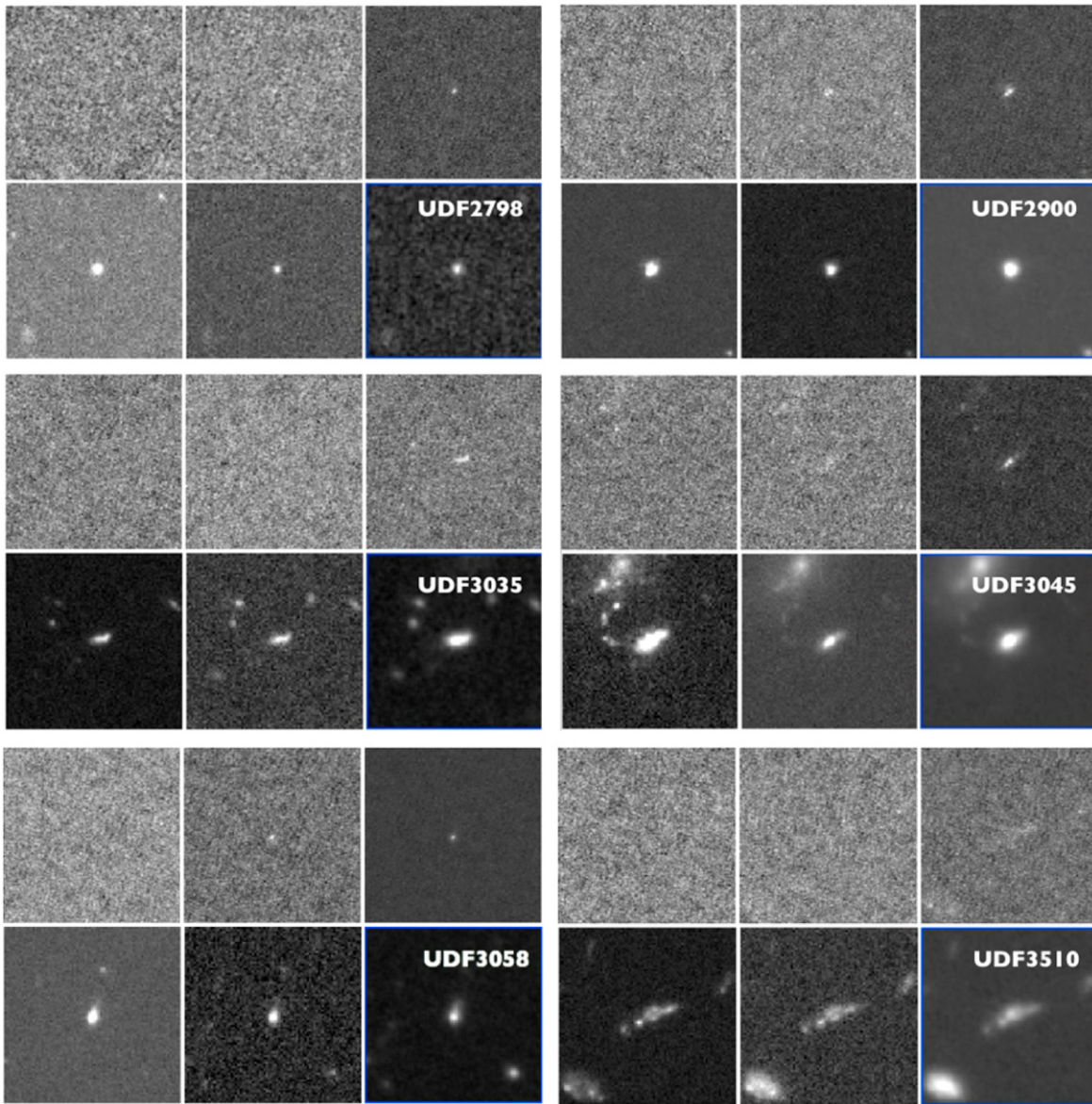
Figure 11. HUDFJ0332.4-2746.6 candidates. For each candidate, starting from the top left, we show clockwise WFC3 $F225W$, $F275W$, and $F336W$ from UVUDF, ACS $F435W$, I_{814}, and WFC3 J_{125} images. Galaxies are identified by their 3D-*HST* ID. The size of each image is $5''$. All candidates are $F275W$ dropouts.

Small samples can hardly be representative of the larger populations, but as with other studies at these high redshifts, we discover new objects often one by one, and we are consistently building larger samples that will improve our understanding of cluster formation and evolution. The CANDELS and 3D-*HST* Treasury programs have opened a new path for proto-cluster detection in this redshift range.

Surveys of this kind point to the capabilities of future space missions, such as Euclid (Laureijs et al. 2011) and WFIRST (Thompson et al. 2013). Those missions have the potential to

Figure 12. HUDFJ0332.4-2746.6 candidates. For each candidate, starting from the top left, we show clockwise WFC3 $F225W$, $F275W$, and $F336W$ from UVUDF, ACS $F435W$, I_{814}, and WFC3 J_{125} images. Galaxies are identified by their 3D-*HST* ID. The size of each image is $5''$. All candidates are $F275W$ dropouts.

discover a large population of young clusters at all redshifts, and especially at these very early epochs of cluster formation and assembly.

Facilities: HST(ACS and WFC3), *Spitzer* (IRAC)

APPENDIX

In Figures 11–13, we show detections and dropouts from the UVUDF survey (Teplitz et al. 2013). Most of the selected galaxies are $F225W$ dropouts, e.g., are not detected in WFC3 $F225W$ (the top left panel), but are detected in WFC3 $F336W$ (the top right panel). The two exceptions are: UDF 1909 and UDF 1898, which are not detected in $F336W$, but are detected in ACS $F435W$, and are most probably at higher redshift galaxies or have too low surface brightness to be unambiguously identified as $z = 1.8-1.9$ galaxies.
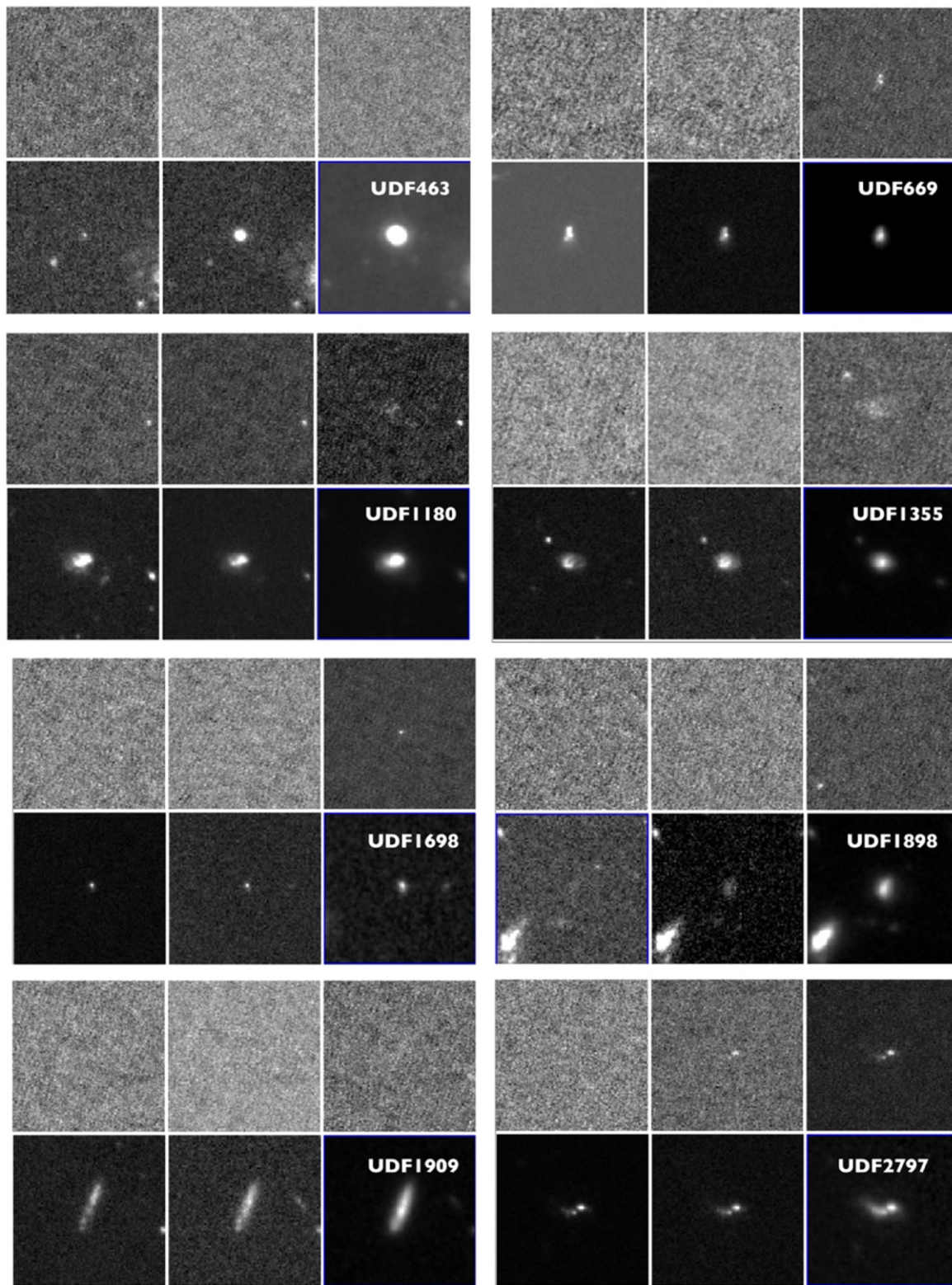
Figure 13. HUDFJ0332.5-2747.3 candidates. For each candidate, starting from the top left, we show clockwise WFC3 $F225W$, $F275W$, and $F336W$ from UVUDF, ACS $F435W$, I_{814}, and WFC3 J_{125} images. Galaxies are identified by their 3D-*HST* ID. The size of each image is 5″. All candidates are $F275W$ dropouts, except for UDF 1909 and UDF 1898. Those two galaxies are not detected in F336W, but are detected in ACS F435W, e.g., they are F435W dropouts. They are excluded from our analysis because they are most probably higher redshift galaxies or have too low surface brightness to be unambiguously identified as $z = 1.8-1.9$ galaxies.

REFERENCES

Andreon, S., & Huertas-Company, M. 2011, A&A, 526, A11
Andreon, S., Maughan, B., Trinchieri, G., & Kurk, J. 2009, A&A, 507, 147
Andreon, S., Newman, A. B., Trinchieri, G., et al. 2014, A&A, 565, A120

Arnouts, S., Moscardini, L., Vanzella, E., et al. 2002, MNRAS, 329, 355
Ashby, M. L. N., Stanford, S. A., Brodwin, M., et al. 2013a, ApJS, 209, 22
Ashby, M. L. N., Stern, D., Brodwin, M., et al. 2009, ApJ, 701, 428
Ashby, M. L. N., Willner, S. P., Fazio, G. G., et al. 2013b, ApJ, 769, 80
Barro, G., Faber, S. M., Pérez-González, P. G., et al. 2013, ApJ, 765, 104

19

Barro, G., Faber, S. M., Pérez-González, P. G., et al. 2014, ApJ, 791, 52
Bassett, R., Papovich, C., Lotz, J. M., et al. 2013, ApJ, 770, 58
Beckwith, S. V. W., Stiavelli, M., Koekemoer, A. M., et al. 2006, AJ, 132, 1729
Bernardi, M., Meert, A., Vikram, V., et al. 2014, MNRAS, 443, 874
Bertin, E., & Arnouts, S. 1996, A&AS, 117, 393
Bird, C. M., & Beers, T. C. 1993, AJ, 105, 1596
Boselli, A., & Gavazzi, G. 2006, PASP, 118, 517
Bouwens, R. J., Illingworth, G. D., Oesch, P. A., et al. 2011, ApJ, 737, 90
Brammer, G. B., van Dokkum, P. G., Franx, M., et al. 2012, ApJS, 200, 13
Brodwin, M., Gonzalez, A. H., Stanford, S. A., et al. 2012, ApJ, 753, 162
Brodwin, M., Stanford, S. A., Gonzalez, A. H., et al. 2013, ApJ, 779, 138
Bruzual, A. G., & Charlot, S. 2003, MNRAS, 344, 1000
Bundy, K., Scarlata, C., Carollo, C. M., et al. 2010, ApJ, 719, 1969
Calzetti, D., Armus, L., Bohlin, R. C., et al. 2000, ApJ, 533, 682
Carlberg, R. G., Yee, H. K. C., Ellingson, E., et al. 1997, ApJL, 485, L13
Castellano, M., Salimbeni, S., Trevese, D., et al. 2007, ApJ, 671, 1497
Castellano, M., Pentericci, L., Menci, N., et al. 2011, A&A, 530, A27
Cautun, M., van de Weygaert, R., Jones, B. J. T., & Frenk, C. S. 2014, MNRAS, 441, 2923
Chabrier, G. 2003, PASP, 115, 763
Chiaberge, M., Capetti, A., Macchetto, F. D., et al. 2010, ApJL, 710, L107
Chiang, Y.-K., Overzier, R., & Gebhardt, K. 2013, ApJ, 779, 127
Cimatti, A., Nipoti, C., & Cassata, P. 2012, MNRAS, 422, L62
Colbert, J. W., Teplitz, H., Atek, H., et al. 2013, ApJ, 779, 34
Cohn, J. D., & White, M. 2005, APh, 24, 316
Conselice, C. J. 2003, ApJS, 147, 1
Cooper, M. C., Newman, J. A., Weiner, B. J., et al. 2008, MNRAS, 383, 1058
Cooper, M. C., Griffith, R. L., Newman, J. A., et al. 2012, MNRAS, 419, 3018
Damjanov, I., Abraham, R. G., Glazebrook, K., et al. 2011, ApJL, 739, L44
Danese, L., de Zotti, G., & di Tullio, G. 1980, A&A, 82, 322
de Lucia, G., & Blaizot, J. 2007, MNRAS, 375, 2
Delaye, L., Huertas-Company, M., Mei, S., et al. 2014, MNRAS, 441, 203
Desai, V., Dalcanton, J. J., Aragón-Salamanca, A., et al. 2007, ApJ, 660, 1151
Dressler, A. 1980, ApJ, 236, 351
Eisenhardt, P. R. M., Brodwin, M., Gonzalez, A. H., et al. 2008, ApJ, 684, 905
Elbaz, D., Daddi, E., le Borgne, D., et al. 2007, A&A, 468, 33
Ellis, R. S., McLure, R. J., Dunlop, J. S., et al. 2013, ApJL, 763, L7
Evrard, A. E., Bialek, J., Busha, M., et al. 2008, ApJ, 672, 122
Fassbender, R., Nastasi, A., Böhringer, H., et al. 2011, A&A, 527, L10
Fazio, G. G., Hora, J. L., Allen, L. E., et al. 2004, ApJS, 154, 10
Fernández Lorenzo, M., Sulentic, J., Verdes-Montenegro, L., & Argudo-Fernández, M. 2013, MNRAS, 434, 325
Galametz, A., Stern, D., de Breuck, C., et al. 2012, ApJ, 749, 169
George, M. R., Ma, C.-P., Bundy, K., et al. 2013, ApJ, 770, 113
Gladders, M. D., & Yee, H. K. C. 2000, AJ, 120, 2148
Gobat, R., Daddi, E., Onodera, M., et al. 2011, A&A, 526, A133
Gobat, R., Strazzullo, V., Daddi, E., et al. 2013, ApJ, 776, 9
Grogin, N. A., Kocevski, D. D., Faber, S. M., et al. 2011, ApJS, 197, 35
Grützbauch, R., Conselice, C. J., Bauer, A. E., et al. 2011, MNRAS, 418, 938
Guo, Q., Ferguson, H. C., Giavalisco, M., et al. 2013, ApJS, 207, 24
Guo, Q., White, S., Boylan-Kolchin, M., et al. 2011, MNRAS, 413, 101
Hahn, O., Porciani, C., Carollo, C. M., & Dekel, A. 2007a, MNRAS, 375, 489
Hahn, O., Carollo, C. M., Porciani, C., & Dekel, A. 2007b, MNRAS, 381, 41
Hatch, N. A., Kurk, J. D., Pentericci, L., et al. 2011, MNRAS, 415, 2993
Hayashi, M., Kodama, T., Koyama, Y., Tadaki, K.-I., & Tanaka, I. 2011, MNRAS, 415, 2670
Hatch, N. A., de Breuck, C., Galametz, A., et al. 2011, MNRAS, 410, 1537
Huertas-Company, M., Tasca, L., Rouan, D., et al. 2009, A&A, 497, 743
Huertas-Company, M., Aguerri, J. A. L., Tresse, L., et al. 2010, A&A, 515, A3
Huertas-Company, M., Aguerri, J. A. L., Bernardi, M., Mei, S., & Sánchez Almeida, J. 2011, A&A, 525, A157
Huertas-Company, M., Mei, S., Shankar, F., et al. 2013a, MNRAS, 428, 1715
Huertas-Company, M., Shankar, F., Mei, S., et al. 2013b, ApJ, 779, 29
Ichikawa, T., Suzuki, R., Tokoku, C., et al. 2006, Proc. SPIE, 6269, 626916
Ilbert, O., Arnouts, S., McCracken, H. J., et al. 2006, A&A, 457, 841
Ilbert, O., Salvato, M., Le Floc'h, E., et al. 2010, ApJ, 709, 644
Illingworth, G. D., Magee, D., Oesch, P. A., et al. 2013, ApJS, 209, 6
Kartaltepe, J. S., Mozena, M., Kocevski, D., et al. 2014, arXiv:1401.2455
Kodama, T., Tanaka, I., Kajisawa, M., et al. 2007, MNRAS, 377, 1717
Koekemoer, A. M., Faber, S. M., Ferguson, H. C., et al. 2011, ApJS, 197, 36
Koekemoer, A. M., Ellis, R. S., McLure, R. J., et al. 2013, ApJS, 209, 3
Koyama, Y., Smail, I., Kurk, J., et al. 2013, MNRAS, 1677
Kuiper, E., Hatch, N. A., Röttgering, H. J. A., et al. 2010, MNRAS, 405, 969
Kuntschner, H., Bushouse, H., Kümmel, M., Walsh, J. R., & MacKenty, J. 2010, Proc. SPIE, 7731

Kurk, J., Cimatti, A., Daddi, E., et al. 2013, A&A, 549, A63
Kurk, J., Cimatti, A., Zamorani, G., et al. 2009, A&A, 504, 331
Laidler, V. G., Papovich, C., Grogin, N. A., et al. 2007, PASP, 119, 1325
Lani, C., Almaini, O., Hartley, W. G., et al. 2013, MNRAS, 435, 207
Laureijs, R., Amiaux, J., Arduini, S., et al. 2011, arXiv:1110.3193
Li, Y., Mo, H. J., van den Bosch, F. C., & Lin, W. P. 2007, MNRAS, 379, 689
Liu, F. S., Guo, Y., Koo, D. C., et al. 2013, ApJ, 769, 147
Lotz, J. M., Papovich, C., Faber, S. M., et al. 2013, ApJ, 773, 154
MacKenty, J. W., & Smith, L. 2012, Proc. SPIE, 8442, 8442N
Mantz, A. B., Abdulla, Z., Carlstrom, J. E., et al. 2014, ApJ, 794, 157
McLean, I. S., Steidel, C. C., Epps, H., et al. 2008, Proc. SPIE, 7014, 70142Z
McLean, I. S., Steidel, C. C., Epps, H. W., et al. 2012, Proc. SPIE, 8446, 84406
Mei, S., Blakeslee, J. P., Stanford, S. A., et al. 2006a, ApJ, 639, 81
Mei, S., Holden, B. P., Blakeslee, J. P., et al. 2006b, ApJ, 644, 759
Mei, S., Holden, B. P., Blakeslee, J. P., et al. 2009, ApJ, 690, 42
Mei, S., Stanford, S. A., Holden, B. P., et al. 2012, ApJ, 754, 141
Merrall, T. E. C., & Henriksen, R. N. 2003, ApJ, 595, 43
Miley, G. K., Overzier, R. A., Tsvetanov, Z. I., et al. 2004, Natur, 427, 47
Miley, G. K., Overzier, R. A., Zirm, A. W., et al. 2006, ApJL, 650, L29
Mortlock, A., Conselice, C. J., Hartley, W. G., et al. 2013, MNRAS, 433, 1185
Munari, E., Biviano, A., Borgani, S., Murante, G., & Fabjan, D. 2013, MNRAS, 430, 2638
Muzzin, A., Wilson, G., Demarco, R., et al. 2013, ApJ, 767, 39
Nakamura, T. K. 2000, ApJ, 531, 739
Navarro, J. F., Frenk, C. S., & White, S. D. M. 1996, ApJ, 462, 563
Newman, A. B., Ellis, R. S., Andreon, S., et al. 2014, ApJ, 788, 51
Newman, A. B., Ellis, R. S., Bundy, K., & Treu, T. 2012, ApJ, 746, 162
Oke, J. B., & Gunn, J. E. 1983, ApJ, 266, 713
Papovich, C., Momcheva, I., Willmer, C. N. A., et al. 2010, ApJ, 716, 1503
Papovich, C., Bassett, R., Lotz, J. M., et al. 2012, ApJ, 750, 93
Peng, C. Y., Ho, L. C., Impey, C. D., & Rix, H. 2002, AJ, 124, 266
Peng, C. Y., Ho, L. C., Impey, C. D., & Rix, H.-W. 2010, AJ, 139, 2097
Pentericci, L., Kurk, J. D., Röttgering, H. J. A., et al. 2000, A&A, 361, L25
Poggianti, B. M., Calvi, R., Bindoni, D., et al. 2013, ApJ, 762, 77
Popesso, P., Biviano, A., Rodighiero, G., et al. 2012, A&A, 537, A58
Postman, M., et al. 2005, ApJ, 623, 721
Raichoor, A., Mei, S., Stanford, S. A., et al. 2012, ApJ, 745, 130
Rettura, A., Rosati, P., Nonino, M., et al. 2010, ApJ, 709, 512
Rigby, E. E., Hatch, N. A., Röttgering, H. J. A., et al. 2013, MNRAS, 2671
Rykoff, E. S., Evrard, A. E., McKay, T. A., et al. 2008, MNRAS, 387, L28
Salimbeni, S., Castellano, M., Pentericci, L., et al. 2009, A&A, 501, 865
Santos, J. S., Fassbender, R., Nastasi, A., et al. 2011, A&A, 531, L15
Santos, J. S., Altieri, B., Tanaka, M., et al. 2014, MNRAS, 438, 2565
Scoville, N., Arnouts, S., Aussel, H., et al. 2013, ApJS, 206, 3
Shankar, F., Marulli, F., Bernardi, M., et al. 2012, MNRAS, 428, 109
Shankar, F., Mei, S., Huertas-Company, M., et al. 2014, MNRAS, 344
Sharples, R., Bender, R., Bennett, R., et al. 2006, NewAR, 50, 370
Shattow, G. M., Croton, G. M., Skibba, G. M., et al. 2013, MNRAS, 433, 3314
Sirianni, M., Jee, M. J., Benítez, N., et al. 2005, PASP, 117, 1049
Snyder, G. F., Brodwin, M., Mancone, C. M., et al. 2012, ApJ, 756, 114
Springel, V., White, S. D. M., Jenkins, A., et al. 2005, Natur, 435, 629
Stanford, S. A., Brodwin, M., Gonzalez, A. H., et al. 2012, ApJ, 753, 164
Steidel, C. C., Adelberger, K. L., Dickinson, M., et al. 1998, ApJ, 492, 428
Strazzullo, V., Gobat, R., Daddi, E., et al. 2013, ApJ, 772, 118
Tadaki, K., Kodama, T., Ota, K., et al. 2012, MNRAS, 423, 2617
Tanaka, M., Finoguenov, A., & Ueda, Y. 2010, ApJL, 716, L152
Tanaka, M., Finoguenov, A., Mirkazemi, M., et al. 2013, PASJ, 65, 17
Teplitz, H. I., Rafelski, M., Kurczynski, P., et al. 2013, AJ, 146, 159
Thomas, D., Maraston, C., Bender, R., & Mendes de Oliveira, C. 2005, ApJ, 621, 673
Thompson, R., Green, J., Rieke, G., et al. 2013, arXiv:1312.4548
Tran, K.-V. H., Papovich, C., Saintonge, A., et al. 2010, ApJ, 719, L126
van Dokkum, P., Brammer, G., Momcheva, I., et al. 2013, arXiv:1305.2140
van der Wel, A., Bell, E. F., Häussler, B., et al. 2012, ApJS, 203, 24
Venemans, B., Röttgering, H. J. A., Miley, G. K., et al. 2007, A&A, 461, 823
Voit, G. M. 2005, RvMP, 77, 207
Vulcani, B., Poggianti, B. M., Oemler, A., et al. 2013, A&A, 550, A58
Wuyts, S., Labbé, I., Schreiber, N. M. F., et al. 2008, ApJ, 682, 985
Wuyts, S., van Dokkum, P. G., Franx, M., et al. 2009, ApJ, 706, 885
White, M., Cohn, J. D., & Smit, R. 2010, MNRAS, 408, 1818
Wylezalek, D., Galametz, A., Stern, D., et al. 2013, ApJ, 769, 79
Yang, X., Mo, H. J., van den Bosch, F. C., et al. 2007, ApJ, 671, 153
Yuan, T., Nanayakkara, T., Kacprzak, G. G., et al. 2014, ApJL, 795, LL20
Xue, Y. Q., Luo, B., Brandt, W. N., et al. 2011, ApJS, 195, 10
Zeimann, G. R., Stanford, S. A., Brodwin, M., et al. 2012, ApJ, 756, 115
Ziparo, F., Popesso, P., Finoguenov, A., et al. 2014, MNRAS, 437, 458